Evidence for Water Ice Near the Lunar Poles

W.C. Feldman[1], S. Maurice[2], D.J. Lawrence[1], R.C. Little[1], S.L. Lawson[1], O. Gasnault[1], R.C. Wiens[1], B.L. Barraclough[1], R.C. Elphic[1], T.H. Prettyman[1], J.T. Steinberg[1], and A.B. Binder[3]

[1]Los Alamos National Laboratory, Los Alamos, New Mexico

[2]Observatoire Midi-Pyrénées, Toulouse, France

[3]Lunar Research Institute, Tucson Arizona

Abstract Improved versions of Lunar Prospector thermal and epithermal neutron data were studied to help discriminate between potential delivery and retention mechanisms for hydrogen on the Moon. Improved spatial resolution at both poles shows that the largest concentrations of hydrogen overlay regions in permanent shade. In the north, these regions consist of a heavily-cratered terrain containing many small (less than about 10 km diameter), isolated craters. These border circular areas of hydrogen abundance ([H]) that is only modestly enhanced above the average equatorial value, but that fall within large, flat-bottomed, and sunlit polar craters. Near the south pole [H] is enhanced within several 30 km-scale craters that are in permanent shade, but is only modestly enhanced within their sunlit neighbors. We show that delivery by the solar wind cannot account for these observations because the diffusivity of hydrogen at the temperatures within both sunlit and permanently-shaded craters near both poles is sufficiently low that a solar wind origin cannot explain their differences. We conclude that a significant portion of the enhanced hydrogen near both poles is most likely in the form of water molecules.

1. Introduction

It was suggested long ago [Watson et al., 1961; Arnold, 1979] that temperatures within permanently shaded regions near the lunar poles were sufficiently low that water delivered to the

Accepted for publication in *Journal of Geophysical Research – Planets*, published 2001

Moon by meteoroids and comets would be stable to sublimation for the lifetime of the Moon. Subsequent refinements to these estimates have supported this conclusion [Butler et al., 1993, 1997; Vasavada et al., 1999]. Experimental support for this suggestion was first presented from an analysis of Clementine radar data [Nozette et al., 1996]. However, analysis of Arecibo radar data [Stacey et al., 1998] and a reanalysis of the Clementine data [Tyler and Simpson, 1999] have raised questions regarding this conclusion. A later analysis of Lunar Prospector (LP) neutron data showed that enhanced abundances of hydrogen, [H], existed at both poles of the Moon [Feldman et al., 1998, 2000a]. Although the spatial resolution of the LP measurements was not sufficiently good to prove a one-to-one correspondence of the signal to the permanently shaded craters near both poles [Margot et al., 1999; Bussey et al., 1999], an association was shown to be plausible. Models of neutron emission from assumed water-ice deposits that filled the largest three craters in the neighborhood of the south pole showed that the Lunar Prospector, (LP), measurements were consistent with a water-ice abundance of 1.5±0.8% by mass. Nevertheless, epithermal neutrons respond to hydrogen regardless of chemical association so an interpretation of the LP data in terms of water ice remains questionable. Indeed, several theoretical analyses [Schmitt and Kulcinski, 1998; Swindle et al., 1992; Starukhina and Shkuratov, 2000; Starukhina, 2000; Crider and Vondrak, 2000] have suggested that the LP data are also consistent with hydrogen atoms delivered to the Moon from the solar wind.

We return to the Lunar Prospector neutron data in the hopes of uncovering additional evidence that could help decide whether any of the polar hydrogen enhancement could be due to water molecules. Our analysis does not preclude the possibility of subsequent evolution through chemical reactions if time and reaction rates permit [Eshleman and Parks, 1999]. Improved spatial resolution is paramount in our new analysis. We have also reworked the epithermal and thermal neutron data in an attempt to minimize their sensitivity to elements other than hydrogen. In the process, we have refined the data using improved corrections for variable gains, sensor temperatures, electronic cross-talk, spacecraft altitudes, cosmic-ray flux variations, the latitude-dependent response function of the neutron spectrometer, and neutron directional aberration

effects due to spacecraft motion. We also incorporate a correction for the latitude-dependent lunar surface temperature [Lawson et al., 2000; Little et al., 2000]. An overview of all corrections to the LP neutron data is given in Section 2. Several maps that define the spatial disposition of hydrogen poleward of $\pm 70^{o}$ latitude are presented in Section 3. Alternate interpretations of these data are contrasted in Section 4, and a discussion of these alternatives is given in Section 5. We conclude that at least some of the enhanced hydrogen deposits inferred from LP epithermal neutron data at both lunar poles is most likely in the form of water molecules.

2. Data Reduction

Since the last publication of LP neutron data [Feldman et al., 2000a], several improvements in our data reduction procedure have been implemented. They include; 1) a better algorithm to account for variations of the flux of galactic cosmic rays that uses the intensity of the 6.13 MeV oxygen gamma-ray line poleward of $+85^{o}$ latitude, 2) correction for temperature variations of the sensors, 3) correction for cross-talk caused by operation of the alpha-particle spectrometer (which is co-located on the same boom as the neutron spectrometer, NS), 4) a new determination of spacecraft vignetting using calibration data measured in lunar orbit (when the spacecraft was in a cart-wheel orientation relative to its polar orbital plane, thereby providing a sensor efficiency that was independent of latitude), 6) use of neutron spin-phase data to determine the variation of effective sensor efficiency with latitude, 7) an improvement of the spatial resolution of the epithermal neutron map by reducing the spatial integration time to 8 s (which corresponds to a 13 km ground track) from 32 s (a 53 km ground track), and 8) use of data measured while in transit from Earth to Moon to remove non-neutron backgrounds. Details of these improvements will be given in a later paper [Maurice et al., in preparation, 2000]. We now believe that the total uncertainties in low-altitude epithermal neutron data poleward of $\pm 70^{o}$ latitude (which includes both systematic and statistical contributions) are less than about 1%.

Another correction to the data, albeit small, is necessary for evaluating the nature of the enhanced hydrogen deposits at the lunar poles. The neutron flux that emerges from the Moon depends on surface temperature. The effect is largest for thermal neutrons but is non-negligible (at the 1% level) for neutrons in the epithermal energy range. Numerical simulations made using the Monte Carlo Neutral Particle transport code (MCNP) from Los Alamos [Little et al., 2000] have shown that the effect at epithermal energies does not depend on soil composition but responds only to the temperature over a range of depths centered at about 30 g cm^{-2} below the surface. A subset of all simulations of neutron flux spectra at 20 g cm^{-2} below the surface for a feldspathic soil composition (here chosen to be ferroan anorthosite, FAN) over the temperature range spanning 25 K to 400 K, are shown in Figure 1a. The thermal peaks are seen to move over an energy range that spans 0.0086 eV to 0.035 eV. Although the effect cannot be seen above E=0.4 eV (which corresponds to the low energy threshold of the LP epithermal NS [Feldman et al., 2000b] in Figure 1a), an expanded version of the energy range between 0.3 and 3 eV shown in Figure 1b, demonstrates a small but significant effect. Little et al. [2000] have verified that this effect stems from a temperature-dependent effect in the total cross section for neutron scattering. Translation of these flux functions to counting rates through use of the simulated detection efficiency (Feldman et al., 2000b] at normal incidence to the LP cadmium-covered ^{3}He counter, (HeCd), yields,

$$C_{HeCd} = 0.027 + 3.28 \times 10^{-6}\ T, \qquad (1)$$

as shown in Figure 2. Here C_{HeCd} is proportional to the counting rate of the HeCd sensor in s^{-1}, and T is the soil temperature (assumed independent of depth) in degrees K. Equation 1 can be used to generate a latitude-dependent correction factor for the measured epithermal neutron flux by using a $\cos^{1/4}\lambda$ dependence of lunar surface temperature on latitude, λ [e.g. Lawson et al., 2000]. Because the sensitive depth of lunar temperature sampled by leakage neutrons falls below the near-surface thermal wave [Vasavada et al., 1999], we choose the temperature profile,

$$T(\lambda) = 250 \cos^{1/4}\lambda , \qquad 100\ K \le T \qquad (2)$$
$$= 100. \qquad T < 100\ K$$

The resulting latitude-dependent correction factor for measured HeCd counting rates is shown in Figure 3. The net pole-to-equator correction factor is seen to be less than 2%. Its credibility is confirmed by the good agreement between the calculated correction factor for thermal neutrons assuming a FAN composition and the latitude dependence of the measured thermal flux over the lunar highlands [Little et al., 2000].

3. Epithermal Neutron Data

Epi* maps of the Moon The intensity of epithermal neutrons provides a very sensitive measure of the hydrogen content of the lunar surface [Lingenfelter et al., 1961]. Basically, neutrons lose energy very rapidly through elastic collisions with protons because the neutron and proton masses are nearly equal and the cross section for elastic scattering is relatively high. This rapid loss leads to a low abundance of neutrons in the epithermal energy range, which, in turn, leads to a low flux of epithermal neutrons that leak outward from the lunar surface.

The epithermal neutron map with lunar temperature effects removed is shown at the top of Plate 1. In our investigation we use a modification of this map that minimizes its resulting sensitivity to abundance variations of all elements other than hydrogen. This was accomplished in Feldman et al [1998, 2000a] by subtracting a fraction of the (temperature-corrected) thermal-neutron counting rates from those for epithermal neutrons. This fraction, g, was determined by minimizing the variance of composite Epi* = [Epithermal – g*Thermal] counting rates measured within each equal-area surface pixel having area equivalent to that of a 2^o longitude by 2^o latitude box at the equator. This procedure yields g=0.057. It differs from that used previously (g≈0.07)

because of the small differences in corresponding data sets (see Section 2). All quantitative estimates of hydrogen abundances in this paper will be made using the Epi* data set.

Epi* data are plotted on an equal-area (equivalent to 0.5^o x 0.5^o equatorial grid) in the bottom panel of Plate 1. Measured counting rates of both the epithermal and Epi* maps were smoothed using a Gaussian algorithm having 40 km FWHM. Inter-comparison shows that much of the signature of mafic terrain that covers the front-side mare and South-Pole Aitken basin, which have dark blue-orange colors, are significantly muted in the Epi* map. In addition, feldspathic terrain that covers the far-side highlands, which have bright yellow-white colors in the epithermal map, are also muted. Indeed, most of the Epi* map equatorward of about $\pm 70^o$ appears as a random salt and pepper pattern of various shades of light and dark orange. Exceptions to this pattern are, 1) generally depressed counting rates at both poles, 2) a pattern of depressed counting rates (shown by patches of blue colors) that surround Imbrium basin, and 3) a group of enhanced counting rates that appear as a pattern of yellow-white patches distributed across the Moon. Whereas the generally depressed counting rates at the poles has been interpreted as enhanced abundances of hydrogen [Feldman et al., 1998, 2000a], the pattern of depressed counting rates surrounding Imbrium basin overlies locations of enhanced KREEP abundance as determined from measured enhancements in the 2.613 MeV gamma-ray line intensity [Lawrence et al., 1999, 2000], and depressions in the thermal neutron flux [Elphic et al., 1998, 1999]. Their interpretation in terms of enhanced Gd and Sm abundances is presented in Maurice et al. [2001].

An attempt to understand the bright patches in terms of regolith maturity (as defined by age and Clementine spectral-reflectance data [Lucey et al., 1998]) was only partially successful [Johnson et al., 2000]. The connection between maturity and epithermal neutron flux is that immature soils should have a low abundance of hydrogen implanted by the solar wind and so should appear bright in epithermal neutrons. The problem here is that some bright areas that would ordinarily be interpreted as regions of high feldspathic composition and/or low [H], overlay mare deposits that lay within ancient formations such as Orientale (20^o S, 95^o W), Moscoviense

(26° N, 147° E), and Tsiolkovskiy (20° S, 129° E). In addition, there are some relatively bright Epi* regions that overlay craters that have no, or very little, mare fill yet are earlier than Copernican. Specific examples are Hausen (66° S, 88° W), Compton (56° N, 105° E), Szilard (34° N, 106° E), Janssen (46° S, 42° E), Sommerfeld (64° N, 193° E), Zeeman (75° S, 134° W), Clavius (58° S, 14° W), and Goldschmidt (73° N, 3° W). This effect can be seen by a close inspection of the full-Moon 750 nm map shown in the top panel of Plate 2, and an overlay of the Epi* and 750 nm maps in the bottom panel. Nevertheless, there are also bright deposits associated with the Copernican craters Tycho (43° S, 11° W) and Jackson (22° N, 164° W). Clearly, there is no simple relationship between early and presumably mature lunar deposits and low Epi* fluxes (which can be associated with enhanced [H]) and late, presumably immature deposits and relatively high Epi* fluxes (associated with low [H]). Nevertheless, a global overview of the Epi* neutron map shows that the interiors of many craters larger than about 100 km diameter are bright relative to their immediate surroundings.

Maps of the Epi* neutron flux poleward of ±70° latitude are shown in Plates 3 and 4. A stereographic projection of the north pole is given in Plate 3 and that of the south pole is in Plate 4. In both plates, the Clementine 750 nm image of the respective pole is positioned next to that of the Epi* map. Concentrating on the north pole first, we see an irregularly shaped domain of generally low intensities at polar latitudes. Its centroid is offset to the back side of the Moon. However, this domain is marked by relatively dark (low Epi* flux - enhanced hydrogen content) and bright (high Epi* flux - low hydrogen content) patches. A close comparison of both the Epi* and 750 nm maps shows that many of the relatively bright patches overlay craters, such as Milankovic (77° N, 170° E), Plaskett (82° N, 175° E), Rozhdestvenskiy (85° N, 150° W), Hermite (86° N, 90° W), Byrd (85° N, 4° E), and Nansen (81° N, 93° E). Inspection of the stereographic projection of the south pole in Plate 4 also shows an irregular pattern of relatively dark and bright patches. A selection of craters that show up as relatively bright patches are Drygalski (79° S, 89° W), Ashbrook (82° S, 115° W), Schrödinger (75° S, 134° E), Goldschmidt (73° N, 5° W), Scott

(82° S, 46° E), Demonax (79° S, 60° E), and Zeeman (75° S, 140° W). This correspondence is demonstrated very clearly by the overlay of LP Epi* and Clementine 750 nm maps in Plate 5.

Further inspection of Plates 3 through 5 shows that the dark regions overlay either craters that harbor regions of permanent shade such as Peary (88° N, 170° E), Shoemaker (88° S, 45° E), Faustini (87° S, 77° E), an unnamed crater at (87° S, 4° W), and Cabeus (84° S,40° W), or inter-crater plains that are covered by a blanket of small craters that harbor floors in permanent shade. Their most visible collection lies at the western intersection of Rozhdestvenskiy and Plaskett [Margot et al., 1999] in the north, and the equatorward rim of Zeeman (72° S, 140° W) in the south.

A global overview of Epi* intensities is summarized in Figure 4. This is accomplished by averaging an ensemble of counting rates within 1° wide polar bands spaced at 10° longitudinal intervals at the equator. The vertical lines at each point give the standard deviations of counting rates within each latitudinal pixel of all 18 polar counting bands. Inspection reveals some important observations. First, subtraction of 5.7% of the thermals from the epithermals to form Epi* does indeed average out all of the variations equatorward of ±70° that are due to composition other than hydrogen. The average Epi* counting rate in low-KREEP regions (defined by a thorium concentration less than 3 ppm) equatorward of about ±75° is about 138 per 8 s. Poleward of ±70° a broad dip in counting rates is observed at both poles, minimizing at a rate of about 130 per 8 s. This decrease amounts to about 6.2% from the equatorward average, which is somewhat larger than values reported previously [Feldman et al., 1998, 2000a]. The new values are more credible because the present data set has incorporated our best estimate of the LPNS latitudinal response and has been checked by a three day calibration run in October, 1998 when the LP spacecraft was operated in a cart-wheel orientation relative to its orbital plane.

The foregoing presentation accentuates the dip in counting rate at both poles relative to those at other locations on the Moon. Whereas the variations over general lunar locations are averaged out in this presentation, those over the poles are not. Comparison of the magnitude of the dip at both poles with the standard deviations of variations at all other lunar locations shows

that the poles do indeed stand out. This fact is demonstrated in Figure 5 where an ensemble of six polar bands is assembled. The particular longitudinal elements of this ensemble were chosen to give both an overview of the individual 1^o-wide bands, and to illustrate several other points that will be presented next. Referring to Plates 1 and 5, the latitude scale in Figure 5 (given by abcissa, L) starts at the longitude, ϕ, (specified in each panel) at the equator in Plate 1. The band first runs north where the latitude at the north pole ($L= 90^o$), passes along the cut in the left-hand panel of Plate 5 that connects ϕ with ϕ-180^o. It then intersects the equator at ϕ-180^o in Plate 1 when the latitude in Figure 5 is $L=180^o$. It then continues to cross the south pole in the right-hand panel of Plate 5 from ϕ-180^o to ϕ where the latitude in Figure 5 is $L=270^o$. Finally, it transits from south to north in Plate 1 at a longitude of ϕ where it intersects the equator at $L=360^o$ in Figure 5.

Starting in the upper left-hand panel of Figure 5, the cut passes first through the south-eastern margin of Imbrium basin at about 15^o N and then close to Aristillus at 33^o N where it encounters high abundances of Gd and Sm [Elphic et al., 2000; Maurice et al., 2001]. Both deposits are marked by a dip in the Epi* counting rate because both Gd and Sm are strong low-energy neutron absorbers that have cross sections that do not follow an $[E]^{-1/2}$ law (like those of the (n,γ) reactions for all of the most abundant elements on the Moon). The sequence of dips and peaks at the north pole correspond to transit through the heavily-cratered northern highlands that contain many small, isolated patches of permanent shade [Margot, et al., 1999], and which correspond to relative minima in Epi* counting rate. It also passes through a linear sequence of large craters (Rozhdestvenskiy, Plaskett, and Milankovic), which correspond to intermediate relative maxima. The depression in Epi* counting rate near the south pole shows a double minimum. The first minimum (very close to the pole) is centered over Shackleton crater and the second at about $L=273^0$ is centered over an unnamed crater found by Margot et al. [1999] and Bussey et al. [1999] to be in permanent shade.

The band shown in the middle panel on the left was chosen because it passes through the center of Rozhdestvenskiy in the north and then over Jackson (a prominent example of a

Copernican crater) on the far side of the Moon at about L=157^{o}. The point to be made here is that the floor of Rozhdestvenskiy is relatively flat and although it is not in permanent shade, it is close to the north pole. It is seen to be marked by an Epi* flux that is lower than the global average, yet is a relative maximum compared to neighboring terrain. On the other hand Jackson is one of the brightest spots on the Moon, having a counting rate that is about 2.4% above the global mean.

The next band (50^{o} East in the lower left-hand panel) was chosen because it passes through Peary crater in the north (L=85^{o}) and Shoemaker crater in the south (L=272^{o}). The Epi* counting rate is minimum over both craters, amounting to about 6.4% and 6.7% below the global mean, respectively. The next band at 80^{o} East (upper right-hand panel) was chosen because it passes through Faustini (L=272^{o}), which was shown to be in permanent shade by Margot et al. [1999] and Bussey et al. [1999]. The Epi* counting rate is seen to minimize here at a level that is 6.7% below the global mean. Proceeding down on the right, the next band at 130^{o} East was chosen because it passes through Cabeus in the south (L=265^{o}). The floor of this crater is also (at least that part that can be seen from Earth) in permanent shade and is marked by a relatively low Epi* counting rate, amounting to 7.5% below the global mean. Finally, the last band at the lower right at 165^{o} East longitude was chosen because it passes through Fra Mauro, Tycho, and the permanently-shaded highlands near the north pole. The minimum in the Epi* counting rate near the north pole amounts to 6.3% below the global mean and that centered on Fra Mauro (L=185^{o}) is 9.0% below the mean. On the other hand, the Tycho complex centered at 42^{o} south latitude (L=222^{o}) is a Copernican feature and has a relative maximum that amounts to 2.7% above the global mean. All of these minima and maxima in percent differences of Epi* counting rates from the global mean, are collected in Table 1.

4. Discussion

Delivery of hydrogen to the lunar poles Detailed examinations of the Epi* maps in Plates 3 through 5 leave little doubt that the minima in counting rates at polar latitudes are strongly associated with terrain that contain many small craters that harbor permanent shade. In contrast, local maxima overlay the floors of large, flat-bottomed craters. We presently do not understand the physical reasons for the local maxima, but the minima have been interpreted in terms of an enhanced abundance of hydrogen [Feldman et al., 1998, 2000a]. Two competing explanations for the enhanced [H] have been given. The first is that hydrogen was delivered episodically to the Moon in the form of water molecules from impacting meteoroids and comets [Watson et al., 1961; Arnold, 1979; Butler et al., 1993, 1997], and retained because of the reduced sublimation rate of H_2O molecules at low temperature. The second is that it was delivered in the form of individual hydrogen atoms coming, at least initially, from the solar wind [Schmitt and Kulcinski, 1998; Swindle et al., 1992; Starukhina and Shkuratov, 2000; Starukhina, 2000; Crider and Vondrak, 2000]. The enhanced [H] then results from a reduction in its loss rate due to the reduced diffusivity of hydrogen implanted in regolith grains at low temperature. Discrimination between these two explanations requires a quantitative analysis of the hydrogen content of polar terrain, followed by a critical analysis of the component parts of the two alternate mechanisms for hydrogen delivery to the poles and its subsequent retention in surface soils.

We start first with a quantitative analysis of [H] near the poles. A comprehensive treatment of the episodic delivery of water molecules to the Moon followed by their subsequent redistribution about the Moon leading to their retention within the various polar cold traps has already been given [Watson et al., 1961; Arnold, 1979; Butler et al., 1993, 1997]. We see no reason to question these analyses so therefore, there is no need to revisit this problem here. However, new data are now available from the ISEE, GEOTAIL, and WIND space-plasma missions that warrant a new appraisal of hydrogen implanted into lunar soil at polar latitudes by the solar wind, magnetosheath, and magnetotail plasmas, which enables a critical discussion of the solar wind origin of lunar [H] deposits and their loss rates. Finally, we give a quantitative

discussion of diffusion in order to intercompare hydrogen loss rates with their delivery rates to provide an estimate of the equilibrium content of hydrogen in lunar soils.

Hydrogen Content of Crater Bottoms Near Both Poles The percent difference of Epi* counting rates from the global average in Table 1 can be translated to hydrogen abundance in ppm by weight, designated w, by referring to Equation 2 in Feldman at al. [1998],

$$\text{Epi*}(w=0) = [1+5.49\text{x}10^{-4}\ w]\ \text{Epi*}(w), \quad (3)$$

which inverts to,

$$w = 18.2\text{x}10^{2}[(\text{Epi*}(0)/\text{Epi*}(w)) - 1]\ . \quad (4)$$

This relation assumes that the abundance of hydrogen on the surface is uniform over an area that is larger than the spatial resolution element of the LP HeCd sensor, and that [H] is low. At high [H], neutron production by galactic cosmic rays is reduced [Drake et al., 1989], an effect that was not included in the ONEDANT simulations of Feldman et al. [1998].

The spatial response function of the LP HeCd sensor was approximated through a series of ONEDANT simulations [Alcouffe et al., 1995] of a small deposit of 3 weight percent water mixed with FAN that was surrounded by dry FAN. A detector having the energy efficiency of the LP HeCd but with an isotropic response function yielded a Gaussian profile given by,

$$R_G(\theta) = \exp[-\theta^2/(2\theta_o^{\,2})], \quad (5)$$

where $\theta_o = 2.57^o$ at an altitude of 100 km. Here, the FWHM = 6.05^o corresponds to a footprint radius of 91.8 km. Integrating Equation 5 over the Moon yields a footprint area of $3.82\text{x}10^4$ km^2. This surface spatial resolution scales directly with spacecraft altitude. Therefore at the altitude of Lunar Prospector in its low-altitude orbit (about 30 km), the FWHM angle, $\theta_o=1.8^o$, corresponds to a footprint radius of 27.5 km and a footprint area of $3.43\text{x}10^3$ km^2. The actual LP

HeCd detector has an angular acceptance that is peaked along the nadir direction near the lunar poles and so should have a footprint that is smaller than that calculated using ONEDANT. Nevertheless, all of the craters having bottoms that are bright in Epi* neutrons in Table 1 have footprint areas that are larger than that of a 60 km diameter circle, and so qualify this criterion.

Inspection of Equation 4 shows that a 1% drop in Epi* counting rates translates to 18.2 ppm of hydrogen. To proceed, though, we need to establish an absolute scale for [H], which translates to establishing Epi*(0). Towards this end, we first note that the procedure used to develop Epi* from the epithermal and thermal neutron counting rates was motivated by the need to produce an index that was as uniquely as possible, sensitive to hydrogen. Comparison of the maps of Epi* and epithermal neutrons in Plate 1 shows that this objective was, for the most part, achieved.

As mentioned previously, a first attempt to interpret the pattern of enhanced Epi* counting rates (yellow-white areas in Plate 1) in terms of regolith maturity ran into mixed results [Johnson et al., 2000]. Whereas some of the bright features (high Epi* counting rates) overlay or border lunar features that have been determined to be relatively recent on lunar evolutionary scales (e.g., Copernican craters such as Tycho, Jackson, Hayn, Bel'kovich K, Giordano-Bruno, and Anaxagoras, [Wilhelms, 1987]), while others cover a wide range of ages earlier than Copernican (such as Janssen (pre-Nectarian), Moscoviense (Nectarian), Orientale (Lower Imbrium), Compton (Lower Imbrium), Tsiolkowsky (Upper Imbrium), and Hausen (Eratosthenian)). Nevertheless, it is reasonable to presume that soils within recently-established lunar features are immature and contain very low [H] when averaged over depths of order one meter, the range of sensitivity of orbital measurements of epithermal neutrons [Feldman et al., 2000b]. Choosing Tycho and Jackson as prototypes because of their relatively large areas, we can tentatively establish these regions as having [H] = 0. Of course, adoption of this interpretation begs the question regarding interpretation of the many older features just mentioned, which are marked by high Epi* counting rates as well. One possibility is that their surface composition is the cause. However, this possibility can be ruled out. Whereas Hausen,

Clavius, Janssen, and most of Compton all appear to have feldspathic composition based on their measured abundance of FeO [Lawrence et al., 2001; Prettyman et al., 2001] and their ratio of thermal to epithermal neutrons (see maps in Feldman et al. [2000b]), Tsiolkovskiy, Moscoviense, and Orientale contain extensive mare deposits and therefore have significant components of mafic composition. A definitive example of the independence of bright features on composition is the broad region of bright Epi* counting rates that cover both Humboldtianum and a large region of neighboring terrain to the north. Here the mare fill of Humboldtianum is both strongly mafic and generally smooth, yet the highland terrain that drapes around the basin to the north is both strongly feldspathic and heavily cratered. Clearly neither composition nor surface roughness can account for bright Epi* features on the Moon. We are therefore forced to conclude that there must be some other common property that prevents their retention of solar wind-implanted hydrogen.

In support of this contention, a survey of all of the 1^{o}-wide bands of Epi* counting rates that were generated (six of which appear in Figure 5) shows that the maximum Epi* counting rate is 3.0% above the global mean at a location given by (46^{o} N, 110^{o} E). We note that this maximum is not much higher than the average of Tycho and Jackson (2.7% and 2.4%, respectively) and is at the 98-percentile level of Epi* counts when averaged over all 2^{o} x 2^{o} spatial-resolution elements (at an altitude of 30 km). If we assume that [H] = 0 for the average of Tycho and Jackson then, use of Equation 4 to estimate $[H]_{ave}$ of low-KREEP terranes equatorward of $\pm 75^{o}$ latitude yields 46 ppm by weight. However, if instead we were to adopt the largest value of Epi* counting rate (3.0% above the global mean) for the standard denoting [H]=0, then the $[H]_{ave}$ is 55 ppm. We note that both estimates must be lower limits because all regolith must contain at least some implanted hydrogen. The closeness of both values to the average hydrogen content determined from samples returned by the Apollo program, $[H]_{ave}$~50 ppm, (see, e.g., Haskin and Warren [1991], and references therein) lends credibility to our assumption. Because [H] must at least be greater than zero, we adopt the 98 percentile level of Epi* as Epi*(0), for the translation of Epi* counts to hydrogen abundances in Table 1. Our

choice of this percentile level to establish [H] = 0 was made to reduce our sensitivity to possible outlier values of Epi* flux intensities in individual spatial pixel elements.

Another factor that might influence the ability of regolith to retain solar wind-implanted hydrogen is temperature. We can evaluate this contribution by comparing our estimates of [H] for the selection of large polar craters given in Table 1, with the estimated temperature of their floors. For those craters that do not harbor sub-craters that contain permanent shade, temperatures can be estimated using the flat-surface approximation studied by Vasavada et al. [1999]. For this case, temperatures depend only on latitude. Diurnal average and maximum temperatures from Figures 12c and 12d of Vasavada et al. [1999] for the examples in Table 1 were used for this purpose, and are given in columns 6 and 8, respectively. Scatter plots of our estimated [H] against crater-bottom temperatures are shown in Figure 6. Although both correlations are not strong (r=0.65 for the maximum temperature and r=0.61 for the average temperature), both are significant. We therefore conclude that polar crater bottoms having lower central temperatures must be able to retain more hydrogen. This result agrees with the impression noted earlier from the Epi* maps presented in Plates 3 through 5.

Arguments that Favor a Solar Wind Origin. The main argument that favors interpretation of the reduced intensity of Epi* rates near the lunar poles in terms of enhanced [H] is that the estimated amount of hydrogen required is quantitatively close [Starukhina and Shkuratov, 2000] to the saturation fluence of 5×10^{17} cm^{-2} measured by Lord [1968]. In this experiment, olivine grains were irradiated with a beam of 2 keV protons. The close equivalence between laboratory and lunar measurements can be demonstrated using the numerical formalism first presented by DesMarais et al. [1974]. If we assume a saturation hydrogen fluence of S_{sat}, that produces a surface-correlated hydrogen abundance in soil grains of W_S, and a volume-correlated hydrogen abundance of W_V (which presumably results from the production of aglutinates during the maturation process [McKay et al., 1991]), then the total hydrogen content, W_H, is given by [DesMarais et al., 1974];

$$W_H = W_S + W_V, \quad (6)$$

where;

$$W_S = 3S_{sat}m_p/(\rho\, r). \quad (7)$$

Here W_H, W_S, and W_V are given in grams per gram, S_{sat} has units of cm^{-2}, m_p is the proton mass in grams, ρ is the specific gravity of the grains, and r is a characteristic length that provides a measure of the ratio of grain volume (V) to surface area (S), r = 3V/S. We can evaluate equations 6 and 7 using the properties of grains in returned lunar samples, $W_V \sim W_S$ [Des Marais et al., 1974], $r \sim 35x10^{-4}$ cm [McKay et al., 1991] and $\rho \sim 2.85$ g cm^{-3} (if we assume a polar composition that is somewhere between a ferroan anorthosite and an anorthositic norite [Wasson and Warren [1980]). We find W_H = 500 ppm by mass.

When one considers the magnitude of the many uncertainties in both this formalism and the values of the parameters that were used in its evaluation, we can only conclude that the resultant abundance of hydrogen it predicts is not sufficiently lower than that inferred from LP Epi* data (for the three large craters near the south pole of the Moon), $W_H = 1700 \pm 900$ ppm [Feldman et al., 2000a], to definitively rule out a solar wind-implantation mechanism. Indeed, we can turn the argument around and ask what grain radius can make the prediction using equations 6 and 7 equal to that estimated from the measured Epi* neutron flux. This exercise yields r ~ 10 microns. As will be seen shortly, our knowledge of the structure of lunar grains at polar latitudes is sufficiently uncertain that r_{ave}=10 microns cannot be ruled out.

Solar Wind Hydrogen Input to the Moon Many estimates of the lunar hydrogen fluence from the solar wind have relied on Apollo-12 ALSEP solar wind data [Neugebauer et al., 1972] and Apollo 12,14, and 15 SIDE data [Hardy et al., 1975]. The most comprehensive model of this fluence was assembled by Swindle et al. [1992]. Their estimate of implanted hydrogen assumed, 1) that not all grain surfaces on the Moon are saturated, and 2) that retention of hydrogen by soil

grains does not depend on chemical composition. Their resultant map of hydrogen input is broadly concentrated at the far-side equator and minimum at both poles, skewed towards the near side. However, inspection of Plates 1 through 5 shows that this prediction is not observed. Clearly, the delivery to, and retention of hydrogen by lunar soils is not dominated by the direct solar wind fluence. Progress in understanding [H] on the Moon therefore requires a step-wise re-evaluation of all hydrogen inputs and the quantitative factors that control its retention. Special attention is given here to the polar regions.

As the model of Swindle et al. [1992] predicts, the direct solar wind input to both poles is about 10% that delivered to the far-side equator. This result follows because, 1) the average thermal Mach number of the flow (which provides a measure of the spreading angle of plasma protons from the bulk-flow direction) is 10.5 (see e.g., Feldman et al. [1978], and references therein), 2) the flow is generally radial away from the Sun with a north-south direction variation of the bulk-flow confined within a FWHM of ±3-degree angle about the ecliptic plane [Wolfe, 1972], and 3) the lunar poles are offset from the normal to the ecliptic plane by only 1.6^{o}. However, flow conditions behind the Earth's bow shock and within the geomagnetic tail at lunar distances differ significantly from that of the upstream solar wind. They may therefore be much more effective in delivering plasma hydrogen to the permanently shaded craters near both poles.

Starting first with flow conditions within the magnetosheath, the most comprehensive survey of the average position of the bow shock and magnetopause was compiled in Figure 2 of Fairfield [1971]. According to this figure, the fraction of the time the Moon spends between the dawn and dusk flanks of the bow shock is 0.302 of its orbital period. Of this period, 0.149 of the time is spent within the magnetosheath and 0.153 of the time is in the magnetotail. According to the measurements made by the LEP experiment aboard Geotail (see Figure 1 of Maezawa and Hori [1998]) the dawn-dusk FWHM extent of the plasma sheet portion of the deep geomagnetic tail (confined by the dawn-dusk flanks of the magnetopause) is about ±25 Earth radii (R_e), which corresponds to 0.137 of a full lunar orbit about the Earth.

The flow state of the magnetosheath at lunar distances is supersonic having a bulk flux, NV_o, that is close to that of the upstream solar wind (see e.g., Petrinec et al. [1997]). However, the thermal Mach number of its flow is less than that of the solar wind. In order to develop a useful average flow state of the magnetosheath at lunar distances, SWE plasma data on WIND were studied over 13 different intervals for a total of 565 hours during 1999 and 2000 [Steinberg et al., in preparation, 2001]. This period occurred during solar maximum and so the flow speed of the solar wind was generally low. Averaging the Mach numbers, <M>, of the flow between 55 and 65 R_e downstream of the Earth, we find <M>=6.1. Averages of other useful parameters of the flow are; 1) the mean proton thermal speed is 72.7 km s^{-1}, 2) the mean proton flux is $2.4x10^8$ cm^{-2} s^{-1}, and the mean proton speed is 420 km s^{-1}. These and other relevant parameters are collected in Table 2.

Conditions in the plasma sheet of the distant geomagnetic tail are characterized by a higher ion temperature and lower Mach number than in the magnetosheath. The most reliable estimates of plasma sheet ion distributions at lunar distances come from measured conditions within the northern and southern flanks of the plasma sheet at about 20 R_e downstream of the Earth. This region maps to the central plasma sheet between 50 and 150 R_e [Borovsky et al., 1998]. Average parameters of an assumed convecting Maxwellian distribution are; a density of $N=10^{-1}$ cm^{-3}, a proton thermal speed of, $V_T=(2kT_p/m_p)^{1/2}$ = 875 km s^{-1}, and a Mach number that is very low. To a very good approximation then, the plasma sheet ion distribution at lunar orbit is isotropic. All parameters are collected in Table 2.

An estimate of the proton flux at both poles, $F(\lambda=\pm 90^o)$, can be made using an assumed Maxwellian velocity distribution:

$$F(\lambda=\pm 90^o) = N[2\pi kT_p/m_p]^{-1/2} \int_{Vmin}^{\infty} V_z \exp[-m_p V_z^2/(2kT_p)]\, dV_z \qquad (8)$$

$$F(\lambda=\pm 90^o) = NV_o/[2\pi^{1/2}M]^{-1} \exp[-m_p V_{min}^2/(2kT_p)] \qquad (9)$$

Where N is the proton number density, V_o is the proton bulk speed, T_p is the proton temperature, m_p is the proton mass, k is Boltzmann's constant, $M = V_o/V_T$, is the thermal Mach number, $V_T=[2kT_p/m_p]^{1/2}$ is the thermal speed, and V_{min} is the minimum speed in the thermal velocity distribution that can impact the center of a crater near the pole. For a crater-free flat surface, $V_{min} = 0$. For a position at the center of a crater near the pole having a depth of d and a diameter of D, $V_{min} = 2dV_o/D = (2d/D)MV_T$. Equation 8 can also be applied to the plasma sheet where the Mach number of the flow is very low. In that case, we get,

$$F_{PS}(\lambda=\pm 90^o) = NV_T/(2\pi^{1/2}). \qquad (10)$$

The foregoing estimates can be generalized to include transverse fluctuations in the bulk flow, $(\delta V^2)^{1/2}$, that result from Alfvén waves. Defining an effective transverse velocity fluctuation of $\delta V^* = [V_T^2 + \delta V^2]^{1/2}$, gives an effective Mach number, $M^* = V_o/\delta V^*$. The resultant polar flux increases because $\delta V^* > V_T$, and M^* decreases, as shown in Table 2.

Time Required to Saturate Regolith Grains We are now in a position to estimate the time required to saturate surface soil grains with hydrogen from plasma distributions downstream of the Earth's bow shock. Starting first for soil grains in the non-shaded portions of the polar regions ($\lambda=\pm 90^o$), the total fluence is given by,

$$FT_{ex} = T_{ex}\,[F_{ms}\,(T_{ms}/T_{ex}) + F_{ps}(T_{ps}/T_{ex})] \qquad (11)$$

Where T_{ex} is the total exposure time, $F_{ms} = 2.4\text{x}10^8/(2\text{x}5.5\,\pi^{1/2}) = 1.2\text{x}10^7$ cm^{-2} s^{-1}, $(T_{ms}/T_{ex})=0.14$, $F_{ps}=(0.1)(8.75\text{x}10^7)/2\pi^{1/2} = 2.5\text{x}10^6$ cm^{-2} s$^{-1,}$ and $(T_{ps}/T_{ex}) = 0.137$. Inserting these numbers into equation 11 we get, $FT_{ex}=T_{ex}(1.68\text{x}10^6 + 0.35\text{x}10^6) = T_{ex}(2.0\text{x}10^6)$ cm^{-2}.

In order to proceed, we need an estimate for the saturation fluence, FT_{ex} at polar latitudes. As mentioned previously, such an estimate is very uncertain because we do not know the

microscopic structure of regolith grains at high latitudes. In fact, we cannot even account for the hydrogen content of returned soil samples from near equatorial regions. Measured hydrogen concentrations are about a factor of 10 below that estimated [Des Marais et al., 1974] for an assumed saturation fluence equal to that measured by Lord [1968] for olivine grains, $FT_{sat} = 5x10^{17}$ cm^{-2}. Nevertheless, our uncertainties regarding the microscopic structure of soils near the poles is sufficiently large that a saturation fluence of 5×10^{17} cm^{-2} cannot be ruled out (see also the analysis of Starukhina and Skhuratov [2000]). We therefore adopt this value, which yields a time required for saturation of $2.5x10^{11}$ s = $7.9x10^3$ years. Note that this time only applies to latitudes of $\pm 90^o$. At more equatorial latitudes, protons from the magnetosheath contribute mainly to the near-side lunar surface, which runs counter to the pattern of retention seen near the north pole in Plates 3 and 5.

To derive the time required to saturate a grain at the center of a permanently shaded crater near the poles, the estimate of the magnetosheath flux needs to be reduced by the factor, $\exp[(-2M*d/D)^2]$. Choosing a crater diameter of D=30 km (which is characteristic of the three prominent permanently-shaded craters near the lunar south pole [Margot et al., 1999]), the crater depth, d, can be estimated using the data in Table 4.1 of Hörz et al. [1991], $d=1.044\ D^{0.301}$ (which for D=30 km), = 0.097D. The reduction factor, $\exp[-(2M*d/D)^2]$ is then 0.31, yielding, $FT_{ex} = T_{ex}(0.87x10^6\ cm^{-2})$, and $T_{ex} = 18x10^3$ years. We note that this time is between 3 and 4 times the average time for a single exposure to the external plasma environment at the surface of the Moon, T_{exp1} = 5000 years [Langevin and Arnold, 1977].

For craters having diameters less than 15 km, d/D=0.2, the reduction factor is 0.0066, and contributions from the magnetosheath should be negligible. The saturation time then becomes $4.4x10^4$ years. Although this time is about nine times the single surface-exposure time of each grain, the estimated number of such exposures is about 30 [Langevin and Arnold, 1977]. Time may therefore still be available to fully saturate all grain surfaces within the permanently shaded craters near the lunar poles. However, the margin of capability is not robust.

Loss Rate due to Sputtering A side benefit of the foregoing analysis is that it allows an estimate of the sputtering rate of water-ice molecules in regions of permanent shade near both poles. Starting first in the north, the reduction factor, $\exp[-(2Md/D)^2]$, is so large for the many small craters having d/D = 0.2 that neither the solar wind nor the magnetosheath contribute significantly to sputtering losses (see Figure 1. of Lanzerotti et al. [1981]). In the south, the reduction factor in the solar wind amounts to 0.016 and that in the magnetosheath amounts to 0.31. Our estimate of the average flux from the solar wind is then about 6×10^6 cm^{-2} s^{-1} and that in the magnetosheath is a factor of 10 lower. These values are sufficiently low that according to Figure 1 of Lanzerotti et al [1981], sputtering losses from the solar wind should compete with sublimation losses only for temperatures below about 100 K, and that from the magnetosheath for temperatures below about 97 K. Of course, these losses only apply during the time that each regolith grain is at the very surface of the Moon, which lasts only about 150,000 years [Langevin and Arnold, 1979]. As shown above, the flux from plasma protons in the plasma sheet at both poles is lower than that in the solar wind by a factor of 10 and so is a negligible source of sputtering losses. Combined with the fact that all sources of sputtering only operate for about 150,000 years (in contrast to the billions of years for sublimation), leads us to conclude that losses to sputtering should not be important. This conclusion is only strengthened if the delivery to, and deposition of hydrogen at both poles is episodic rather than continuous [Arnold, 1979].

Penetration Depths of Plasma Protons The average kinetic energy of plasma protons in the solar wind and magnetosheath at lunar distances is about 1 keV. Occasional penetration of Earth's orbit into the polar solar wind or flare ejecta can expose lunar surface material to ~4 keV protons. However, in the plasma sheet at lunar distances the average proton thermal energy is about 4 keV all of the time. Use of this energy to estimate the thickness of material penetrated by plasma protons yields about 6×10^{-6} cm (see, e.g., Johnson [1990]). Because all ions in the lunar environment have nearly equal bulk and thermal speeds, the depth of damaged lattices that

define the amorphous coats that surround each regolith grain is dominated by heavy ions, which amounts to about twice the proton penetration depth, or about 10^{-5} cm [Bibring et al., 1972].

Diffusion of Surface Implanted Hydrogen Hydrogen atoms will diffuse both into and out of regolith grains after implantation from the neighboring plasma environment. The rate of diffusion will depend both on the mineral composition of the grain [Jull and Pillinger, 1977], its radiation damaged lattice structure [Chen and Gonzales, 1993], and the temperature (see e.g., Wang et al. [1996] and references therein). The effects of this diffusion are well documented for soil samples returned by the Apollo and Luna missions [e.g. Leich et al., 1974]. Non-negligible amounts of hydrogen are observed at depths as great as several times 10^{-5} cm, a distance beyond the initial penetration depths of plasma protons. The effect of this process is very important for determining the amount of hydrogen eventually retained by each regolith grain. Indeed, the implantation into, and retention of hydrogen by individual grains depends on the competition between several processes whose differing time scales regulate the structure of the outer layers of these grains. These scales include; 1) the deposition time to reach initial saturation, 2) the diffusion time that regulates ion mobility after implantation, 3) the mean life of a grain at the lunar surface for each single exposure to the plasma environment, 4) the total time spent at the lunar surface, 5) the time spent within the outer skin of the soil (about 2 cm thickness [Vasavada et al., 1999]) that undergoes large diurnal temperature variations, and 6) the time scale of a given orientation of the lunar poles relative to the heliocentric radial. These scales are collected in Table 3.

Several of these scales are interdependent. For example, the diffusion time depends on the amount and type of radiation damage and the resultant structure of regolith-grain skins. However, skin structure depends on the competition between the input flux of protons and micrometeoroids as well as the diffusion rate of implanted hydrogen. If the input rate sufficiently exceeds the diffusion rate, gas bubbles will form, which will lead to blistering and eventual loss to ruptures in the outer skin [McCracken, 1975]. The blistered skins have a

thickness comparable to the initial penetration depth of plasma protons, ~10^{-5} cm. However, at more moderate input rates, the evolution of the amorphous outer skin is controlled by sputtering loss caused by plasma bombardment, and ablation caused by micrometeoroids. Clearly, the evolution of lunar regolith grains is very complicated. There is, at present, no quantitative theory that can predict equilibrium structure from given input conditions. We have therefore only a qualitative descriptive knowledge based on returned samples from near equatorial latitudes. Extrapolation to polar latitudes, which are characterized by much lower temperatures and hence increased diffusion times, can likewise be, at best, qualitative.

Characteristic diffusion times are given by [e.g., Crank, 1975],

$$T_d = d_p^2 \exp[Q/(RT_g)]/(4D_o) \qquad (12)$$

where d_p is the characteristic penetration distance, chosen here to be $d_p = 0.5\ 10^{-5}$ cm, D_o is the diffusion coefficient at infinite temperature, Q is the activation energy of hydrogen in the mineral lattice, R is the universal gas constant, R = 8.3 Joule, K^{-1} $(g\ mole)^{-1}$, and T_g is the absolute grain temperature in degrees K. Values for D_o and Q for various minerals that have appeared in the published literature are collected in Table 4. Plots of $\log_{10}T_d$ as a function of $100/T_g$ for T_g between 100 K and 500 K are shown in Figure 7. The units of T_d are in billions of years so that an ordinate of 1 (10 b.y.) is longer than the age of the Moon. We note from the figure that the temperature dependence of all diffusion times is extreme (all lines are nearly vertical). This fact translates to large differences in diffusion times for small differences in temperature.

In order to evaluate the role that diffusion plays in determining the equilibrium hydrogen content of lunar soils, we need to concentrate on only those minerals that are found in abundance on the Moon. The lone trace on the right of Figure 7 (which is characterized by the highest diffusivity) is not important because it was measured along the c axis of rutile and so was strongly influenced by channeling. Not only is rutile not abundant on the Moon, but the layer in which hydrogen is implanted in all regolith grains is amorphous so that channeling is not

important. The next most diffusive mineral in Figure 7 is rhyolite, which, along with quartz, is also not abundant on the Moon. The remaining five minerals, olivine, potassium feldspar, pyrope, basalt melt, and diopside do indeed contribute in varying proportions to different surface lithologies. Although olivine is not a major constituent of polar soils, which are primarily feldspathic in composition, we can determine upper limits to the diffusivity of hydrogen by using the diffusion time for olivine (given by solid circle symbols in Figure 7). These times were estimated for all of the entries in Table 1 using Equation 12. The results are collected in columns 7 and 9 of Table 1 for the estimated average and maximum temperatures, respectively. Scatter plots of [H] at the centers of all large polar craters against the appropriate diffusion times are shown in Figures 8a and 8b. The times for the maximum temperature were all adjusted upward in Figure 8a by a factor of two to approximate the fact that this temperature is only recorded for less than half of each lunar day.

Assessment of the role that diffusion plays in the equilibrium retention of hydrogen by regolith grains must start first with the maximum temperature estimates. The time scale for which these conditions are effective is the gardening time for turnover down to 2 cm. This level is the depth below which diurnal temperature swings are strongly attenuated by the low conductivity of surface soils [Vasavada et al., 1999]. An estimate for the gardening time for 2 cm was given by Gault et al. [1974] as 10 M.y. However, only five of the 14 craters of our polar sample have maximum temperatures sufficiently high that diffusion times are shorter than 10 M.y. Inspection of Figure 8a shows that the hydrogen contents of these craters are not correlated with their estimated diffusion times. Diffusion can therefore not be an important factor in establishing their equilibrium hydrogen abundance. This conclusion is reinforced by inspection of the scatter plot in Figure 8b. The time scale of importance here is that of the orientation of the lunar pole relative to the ecliptic plane, which is estimated to be of order 2 to 3 b.y. [Ward, 1975]. However, diffusion time scales for average temperatures in all of the polar craters under study here are far larger than 3 b.y. (which would correspond to 0.5 on the abcissa of Figure 8b). The only possible escape from this conclusion is the possibility that there may be a mechanism

for diffusion at low temperatures that dominates over those measured in the laboratory at temperatures higher than 400 K. This mechanism would have to be characterized by very low diffusion coefficients and activation energies.

5. Summary and Conclusions

Lunar Prospector epithermal neutron data were studied to evaluate the probable chemical state of enhanced hydrogen reported previously to be near both lunar poles [Feldman et al., 1998, 2000a]. The present versions of thermal and epithermal neutron data are significantly improved over those used previously, as outlined in section 2. Most important is the improved spatial resolution obtained by using our 8 s data as distinct from the 32 s data used previously. However, many small corrections for time variations due to instrumental drifts, use of in-flight calibration data to determine the latitudinal dependence of sensor efficiency and spatial response function, and correction for the temperature (and hence latitude) dependence of measured neutron flux, were important also. A new composite data set was created, Epi* = [Epithermal – 0.057xThermal], to reduce effects of composition variations other than hydrogen. Although this new composite was seen to be generally effective in Plate 1, sensitivity to abundance variations in Gd and Sm are seen in terrain that neighbors Imbrium basin (see, e.g., Maurice et al. [2001]).

Comparison of maps of Epi* counts with the Clementine 750 nm photon intensity reveal a strong correspondence between distinguishing features in both data sets. The Epi* counting rates are generally low near both lunar poles and high over terrain near recent impact events such as Tycho, Jackson, Hayn, Anaxagorus, and Giordano-Bruno. However, other lunar features are also associated with high Epi* rates, which represent a wide range of terrain types that seem to have nothing in common. For example, lunar features characterized by high Epi* rates span the full range of ages (from pre-Nectarian through Copernican), contain the full range of compositions that span ultra mafic (e.g., Tsiolkowskiy) to feldspathic (e.g., Hausen), and that span the full range of fine-scale spatial structure, that range between a smooth mare surface (e.g.,

Humboldtianum) and a rugged, highly-cratered highland terrain (that neighboring Hayn, Bel'kovich, and Compton). Nevertheless, if we postulate that one property all bright Epi* features have in common is a low hydrogen abundance (regardless of the fact that we do not yet know why) then measured Epi* counting rates appear to be quantitatively self consistent. If we define the abundance of hydrogen near Tycho and Jackson to be zero, then the average hydrogen content of KREEP-poor soils equatorward of $\pm 75^{o}$ is 46 ppm. If instead, we assume that [H]=0 within the feature having an Epi* counting rate at the +98-percentile level averaged over all 2^{o} x 2^{o} spatial resolution elements, then $[H]_{ave}$ = 55 ppm. Both values compare favorably with the average found in returned lunar soil samples, $[H]_{ave} \sim 50$ ppm [Haskin and Warren, 1991].

Using the foregoing physical interpretation of Epi* counting rates, we find that [H] within most of the large craters poleward of $\pm 70^{o}$ is lower than that in neighboring inter-crater terrain. Fourteen craters having areas larger than the LP epithermal spatial response function (55 km diameter at 30 km altitude) were singled out for study. Although [H] generally increased with decreasing distance from the pole (and hence decreasing temperature), quantitative estimates of the diffusivity of hydrogen at low temperatures showed that diffusion cannot be an important factor. Hydrogen implantation from the solar wind does not, therefore, seem able to explain the difference between the hydrogen content observed within the large sunlit polar craters and the neighboring inter-crater terrain.

A closer look at the 'inter-crater' plains just mentioned shows that they are covered by many small craters that harbor floors in permanent shade (Margot et al., 1999; Bussey et al., 1999]. The floor temperatures within these craters are significantly lower than those predicted for neighboring terrain that receives at least some sunlight (see e.g., Vasavada et al. [1999]). If these temperatures are cold enough, they can disable sublimation of water ice as a viable loss process. It is therefore tempting to postulate that the enhanced hydrogen within regions of permanent shade is in the form of water molecules. This postulate is certainly viable within the bottoms of craters near the south pole (such as Shoemaker, Faustini, an unnamed crater near (87.5^{o} N, 4^{o} W), and Cabeus). These craters are sufficiently large that predicted temperatures

within them fall well below 100 K, that needed to stabilize water ice for billions of years (see, e.g., Vasavada et al. [1999]).

The picture is different in the north. Here, there are relatively few permanently-shaded craters that are large enough to harbor temperatures that are sufficiently low to stabilize water ice against sublimation [Vasavada et al., 1999]. Instead, the 'inter-crater' polar terrain is a jumble of small craters (diameters less than 10 km) that harbor permanent shade [Margot et al., 1999]. Although simulations of temperatures within this class of craters are only marginally cold enough to stabilize water ice against sublimation [Vasavada et al., 1999], this terrain appears to contain the highest hydrogen concentration. Nevertheless, predicted temperatures are close enough as to suggest strongly that sublimation is indeed the process that discriminates between polar terrain that contain enhanced hydrogen and those that do not (see also the analysis of Carruba and Coradini [1999] for doubly-shaded craters). If correct, then an important fraction of the hydrogen near the north pole must reside within these small craters.

Estimates of the water fraction of floor-bottom soils near the south pole from our present analysis remain unchanged from that of our previous analysis [Feldman et al., 2000a], [H] = 1700±900 ppm. This translates to $[H_2O]$=1.5±0.8%. If all of the enhanced hydrogen in the north is in the form of H_2O and is confined to the jumble of small permanently-shaded craters identified by the radar study of Margot et al. [1999], then we can estimate their water-ice fraction, $[H_2O]$, using Figure 1 of Feldman et al. [2000a]. We chose two regions near the north pole for this purpose. They each have areas just larger than the surface foot-print of the LP epithermal neutron spectrometer. The first was an inter-crater region nestled between Rozhdestvenskiy and Plaskett, and the second covered the southeast corner of Peary. Using Figure 3 of Margot et al. [1999], the first area contained 232 km^2 of measured permanent shade, and the second contained 129 km^2. Although we do not have enough information to make a realistic estimate of the total amount of shaded area in each region, we can adopt the prescription used by Margot et al. [1999] in their Table 1. We therefore multiplied each by 1.5. This yields estimated areas in permanent shade that amount to 350 km^2 in region 1, and 200 km^2 in the

southeast corner of Peary. Comparison of the Epi* counts for both regions (given in the fourth column of Table 1), with the curves in Figure 1a of Feldman et al. [2000a] yields an estimated water-ice fraction greater than 10%. We judge that it is not worth the effort to refine this estimate because of its sensitivity to our estimate of permanently-shaded area, which is very uncertain. However, we note that if correct, this weight fraction (when converted to [H]) is significantly higher than what can be delivered to, and retained by the lunar polar terrain, from the solar wind. Thus regardless of whether there exists additional high diffusivity mechanisms that dominate diffusion at the low temperatures reached at polar latitudes, the foregoing estimated large [H] weight fractions by themselves, rules in favor of the existence of significant water ice deposits at both lunar poles.

Acknowledgments We wish to thank J. Borovsky and M. Thomsen for many conversations regarding estimates of the plasma proton contribution to polar hydrogen from the plasma sheet and magnetosheath, respectively. Work at Los Alamos was carried out under the auspices of the U.S. Department of Energy and financial support from NASA through Lunar Research Institute. Support for S. Maurice was provided by the Observatoire Pic Midi.

References

Alcouffe, R.E., R.S. Baker, F.W. Brinkely, D.R. Marr, R.D. O'Dell, W.F. Walters, DANTSYS: A diffusion accelerated neutral particle transport code system, LANL Manual LA-12969-M, Los Alamos Natl. Lab., Los Alamos, N.M., 1995.

Arnold, J.R., Ice in the lunar polar regions, J. Geophys. Res., 84, 5659-5668, 1979.

Bibring, J.P., J. Borg, A.L. Burlingame, Y. Langevin, M. Maurette, B. Vassent, Solar-wind and solar-flare maturation of the lunar regolith, Prc. Lunar Sci. Conf. 6th, 3471-3493, 1975.

Borovsky, J.E., M.F. Thomsen, R.C. Elphic, T.E. Cayton, D.J. McComas, The transport of plasma sheet material from the distant tail to geosychronous orbit, J. Geophys. Res., 103, 20297-20331, 1998.

Bussey, D.B.J., P.D. Spudis, M.S. Robinson, Illumination conditions at the lunar south pole, Geophys. Res. Lett. 26, 1187-1190, 1999.

Butler, B.J., D.O. Muhleman, M.A. Slade, Mercury: full-disk radar images and the detection and stability of ice at the north pole, J. Geophys. Res., 98, 15003-15023, 1993.

Butler, B.J., The migration of volatiles on the surfaces of Mercury and the Moon, J. Geophys. Res., 102, 19283-19291, 1997.

Carruba, V., A. Coradini, Lunar cold traps: effects of double shielding, Icarus, 142, 402-413, 1999.

Chen, Y., M.M. Abraham, H.T. Tohver, Radiation-induced diffusion of hydrogen and deuterium in MgO, Phys. Rev. Lett., 37, 1757-1760, 1976.

Crank, J., 'The Mathematics of Diffusion', Clarenden Press, Oxford, 1975.

Crider, D.H., R.R. Vondrak, The solar wind as a possible source of lunar polar hydrogen deposits, J. Geophys. Res., 105, 26773-26782, 2000.

DesMarais, D.J., J.M. Hayes, W.G. Meinschein, The distribution in lunar soil of hydrogen released by pyrolysis, Geochim. Cosmo. Acta, 2, 1811-1822, 1974.

Drake, D.M., W.C. Feldman, B.M. Jakosky, Martian neutron leadage spectra, J. Geophys. Res., 93, 6353-6368, 1988.

Elphic, R.C., D.J. Lawrence, W.C. Feldman, B.L. Barraclough, S. Maurice, A.B. Binder, P.G. Lucey, Lunar Fe and Ti abundances: comparison of Lunar Prospector and Clementine data, Science, 281, 1493-1496, 1998.

Elphic, R.C., D.J. Lawrence, W.C. Feldman, B.L. Barraclough, S. Maurice, A.B. Binder, P.G. Lucey, Lunar rare earth element distribution and ramifications for FeO and TiO_2: Lunar Prospector neutron spectrometer observations, J. Geophys. Res., 105, 20333-20345, 2000.

Eshleman, V.R., G.A. Parks, No ice on the Moon?, Science, 285, 531-532, 1999

Fairfield, D.H., Average and unusual locations of the Earth's magnetopause and bow shock, J. Geophys. Res., 76, 6700-6716, 1971.

Feldman, W.C., J.R. Asbridge, S.J. Bame, J.T. Gosling, Plasma and magnetic fields from the Sun, in 'The Solar Output and its Variation, O.R. White, Ed., Colorado Assoc. Univ. Press, Boulder, pp351-382, 1977.

Feldman, W.C., S. Maurice, A.B. Binder, B.L. Barraclough, R.C. Elphic, D.J. Lawrence, Fluxes of fast and epithermal neutrons from Lunar Prospector: evidence for water ice at the lunar poles, Science, 281, 1496-1500, 1998.

Feldman, W.C., D.J. Lawrence, R.C. Elphic, B.L. Barraclough, S. Maurice, I. Genetay, A.B. Binder, Polar hydrogen deposits on the Moon, J. Geophys. Res., 105, 4175-4195, 2000a.

Feldman, W.C., D.J. Lawrence, R.C. Elphic, D.T. Vaniman, D.R. Thomsen, B.L. Barraclough, S. Maurice, A.B. Binder, Chemical information content of lunar thermal and epithermal neutrons, J. Geophys. Res., 105, 20347-20363, 2000b.

Gault, D.E., F. Hörz, D.E. Brownlee, J.B. Hartung, Mixing of the lunar regolith, Proc. Lunar Planet. Sci. Conf. 5th, 2365-2386, 1974.

Hardy, D.A., H.K. Hills, J.W. Freeman, A new plasma regime in the distant geomagnetic tail, Geophys. Res. Lett., 2, 169-172, 1975.

Haskin, L., P. Warren, Lunar chemistry, in 'Lunar Sourcebook, a User's Guide to the Moon', G. Heiken, D. Vaniman, B.M. French, eds., pp 357-474, 1991.

Hörz, F., R. Grieve, G. Heiken, . Spudis, A. Binder, Lunar surface processes, in 'Lunar Sourcebook, a User's Guide to the Moon', G. Heiken, D. Vaniman, B.M. French, eds., pp 61-120, 1991.

Ingrin, J., S. Hercule, T. charton, Diffusion of hydrogen in diopside: results of dehydration experiments, J. Geophys. Res., 100, 15489-15499, 1995.

Johnson, J.R., S. Maurice, W. Feldman, P.G. Lucey, T.D. Swindle, Correlations among epithermal* neutrons, hydrogen content, and surface features outside the polar regions, Proc. Of the New Views of the Moon III, Lun. Plan. Inst., Houston, 12-15 Oct., 2000.

Johnson, O.W., J.W. Deford, S.-H. Paek, Concentration dependent diffusion of H^+ in TiO_2: analysis of electronic effects in ionic diffusion, Materials Science Res., 9, 253-267, 1975.

Johnson, R.E., 'Energetic Charged-Particle Interactions with Atmospheres and Surfaces', Springer-Verlag, Berlin, 232 pp., 1990.

Jull, A.J.T., C.T. Pillinger, Effectof of sputtering on solar wind element accumulation, Proc. Lunar Sci. Conf. 8^{th}, 3817-3833, 1977.

Kats, A., Y. Haven, J.M. Stevels, Hydroxyl groups in α-quartz, Phys. And Chem. Of Glasses, 3, 69-75, 1962.

Kronenberg, A.K., S.H. Kirby, R.D. Aines, G.R. Rossman, Solubility and diffusional uptake of hydrogen in quartz at high water pressures: implications for hydrolytic weakening, J. Geophys. Res., 91, 12723-12744, 1986.

Kronenberg, A.K., G.R. Rossman, R.A. Yund, A.R. Huffman, EOS, 70, 1406, 1989

Langevin, Y., J.R. Arnold, The evolution of the lunar regolith, Ann. Rev. Earth Planet Sci. 5, 449-489, 1977.

Lanzerotti, L.J., W.L. Brown, R.E. Johnson, Ice in the polar regions of the Moon, J. Geophys. Res., 86, 3949-3950, 1981.

Lawson, S.L., B.M. Jakosky, H.-S. Park, M.T. Mellon, Brightness temperatures of the lunar surface: calibration and global analyssi of the Clementine long-wave infrared camera data, J. Geophys. Res., 105, 4273-4290, 2000.

Lawrence, D.J., W.C. Feldman, B.L. Barraclough, A.B. Binder, R.C. Elphic, S. Maurice, D.R. Thomsen, High resolution measurements of absolute therium abundances on the lunar surface, Geophys. Res. Lett., 26, 2681-2684, 1999.

Lawrence, D.J., W.C. Feldman, B.L. Barraclough, A.B. Binder, R.C. Elphic, S. Maurice, M.C. Miller, T.H. Prettyman, Thorium abundances on the lunar surface, J. Geophys. Res., 105, 20307-20331, 2000.

Lawrence, D.J., W.C. Feldman, D.T. Blewett, R.C. Elphic, P.G. Lucey, S. Maurice, T.H. Prettyman, A.B. Binder, Iron abundance on the lunar surface as measured by the Lunar Prospector gamma-ray spectrometer, Lunar Planet. Sci. Conf. XXXII, Abstract # 1830, 2001.

Leich, D.A., R.H. Goldberg, D.S. Burnett, T.A. Tombrello, Hydrogen and fluorine in the surfaces of lunar sample, Geochim. Cosmo. Acta, 2, 1869-1884, 1974.

Lingenfelter, R.E, E.H. Canfield, W.N. Hess, The lunar neutron flux, J. Geophys. Res., 66, 2665-2671, 1961.

Little, R.C., W.C. Feldman, D.J. Lawrence, S. Maurice, Temperature dependence of thermal neutrons from the Moon, Los Alamos Res. Rep., LAUR-003125, 2000.

Lord, H.C., Hydrogen and helium ion implantation into olivine and enstatite: retention coefficients, saturation concentrations, and temperaute-release profiles, J. Geophys. Res., 73, 5271-5280, 1968.

Lucey, P.G., D.T. Blewett, B.R. Hawke, Mapping the FeO and TiO_2 content of the lunar surface with multispectral imagery, J. Geophys. Res., 103, 3679-3699, 1998.

Mackwell, S.J., D.L. Kohlstedt, J. Geophys. Res., 95, 5079-5088, 1990.

Maezawa, K., T. Hori, The distant magnetotail: its structure, IMF dependence, and thermal properties, in 'New Perspectives on the Earth's Magnetotail', A. Nishida, D.N. Baker, S.W.H. Cowley, eds., Geophys. Mono. 105, AGU Press, Wash. DC, pp. 1-19, 1998.

Margot, J.L., D.B. Campbell, R.F. Jurgens, M.A. Slade, Topography of the lunar poles from radar interferometry: a survey of cold trap locations, Science, 284, 1658-1660, 1999.

Maurice, S., W.C. Feldman, C. D'Uston, R.C. Elphic, I. Genetay, D.J. Lawrence, A.B. Binder, Detection of rare-Earth elements with the Lunar Prospector epithermal neutron detector, J. Geophys. Res., submitted, 2001.

McCracken, G.M., The behaviour of survaces under ion bombardment, Rep. Prog. Phys. 38, 241-327, 1975.

McKay, D.S., G. heiken, A. Basu, G. Blanford, S. Simon, R. Reedy, B.M. French, J. Papike, The Lunar Regolith, in 'Lunar Sourcebook, a User's Guide to the Moon', G. Heiken, D. Vaniman, B.M. French, eds., pp 285-356, 1991.

Neugebauer, M., C.W. Snyder, D.R. Clay, B.E. Goldstein, Solar wind observations on the luanr surface with the Apollo-12 ALSEP, Planet. Space Sci. 20, 1577-1591, 1972.

Nozette, S., C.L. Lichtenberg, P. Spudis, R. Bonner, W. Ortr, E. Malaret,, M. Robinson, E.M. Shoemaker, The Clementine bi-static radar experiment,j Science, 274, 1495-1498, 1996.

Petrinec, S.M., T. Mukai, A. Nishida, T. Yamamoto, T.K. Nakamura, Geotail observations of magnetosheath flow near the magnetopause using Wind as a solar wind monitor, J. Geophys. Res., 102, 26943-26959, 1997.

Prettyman, T.H., W.C. Feldman, D.J. Lawrence, R.C. Elphic, O. Gasnault, S. Maurice, K.R. Moore, A.B. Binder, Distribution of iron and titanium on the lunar surface from Lunar Prospector gamma ray spectra, Lunar Planet. Sci. Conf. XXXII, Abstract # 2122, 2001.

Schmitt, H.H., G.L. Kuscinski, Premature lunar assumptions, Space News, 9, 23-24, 1998.

Simpson, R.A., G.L. Tyler, Reanalysis of Clementine bistatic radar data from the lunar south pole, j. Geophys. Res., 104, 3845-3862, 1999.

Stacey, N.J.S., D.B. Campbell, P.G. Ford, Arecibo radar mapping of the lunar poles: a search for ice deposits, Science 276, 1527-1530, 1997.

Starukhina, L.V., Y.G. Shkuratov, The lunar poles: water ice or chemically trapped hydrogen?, Icarus, 147, 585-587, 2000.

Starukhina, L.V., The excess hydrogen on the lunar poles: water ice or chemically trapped solar wind? Lunar Planet. Sci. Conf., XXXI, 2000.

Swindle, M.K. Burlkand, j.R. Johnson, S.M. Larson, R.V. Morris, B. Rizk, R.B. Singer, Systematic variations in solr wind fluence with lunar location: implications for abundances of solar wind implanted volatiles Lunar Planet. Sci. Conf. XXIII, 1395-1396, 1992.

Vasavada, A.R., D.A. Paige, S.E. Wood, Near-surface temperatures on Mercury and the Moon and the stability of polar ice deposits, Icarus, 141, 179-193, 1999.

Wang, L. Y.Zhang, E.J. Essene, Diffusion of the hydrous component in pyrope, Amer. Miner. 81, 706-718, 1996.

Ward, W.R., Past orientation of the lunar spin axis, Science, 189, 377-379, 1975.

Wasson, J.T., P.H. Warren, Contribution of the mantle to the lunar asymmetry, Icarus, 44, 752-771, 1980.

Watson, K., B.C. Murray, H. Brown, The behavior of volatiles on the lunar surface, J. Geophys. Res., 66, 3033-3045, 1961.

Wilhelms, D.E., ‘The Geologic History of the Moon, U.S. Geol. Surv. Prof. Paper, 1348, 1987.

Wolfe, J.H., The large-scale structure of the solar wind,in ‘Solar Wind’, C.P. Sonett, P.J. Coleman, Jr., J.M. Wilcox, Eds., NASA Publ., Wash. D.C., pp170—201, 1972.

Zhang, Y., E.M. Stolper, Water diffusion in basaltic melts, Nature, 351, 306-309, 1991.

Zhang, Y., E.M. Stolper, G.J. Wasserburg, Diffusion of water in rhyolitic glasses, Geochim. Cosmochim. Acta, 55, 441-456, 1991.

Figure Captions

Plate 1. Full-Moon latitude-longitude maps of the epithermal (top) and Epi* neutron counting rates (bottom).

Plate 2. Full-Moon latitude-longitude maps of the Clementine 750 nm intensity (top) and an overlay of the Epi* neutron flux and 750 nm intensity maps (bottom).

Plate 3. Stereographic projections of the Epi* flux (left) and Clementine 750 nm intensity (right) poleward of $+70^{o}$ latitude.

Plate 4. Stereographic projections of the Epi* flux (right) and Clementine 750 nm intensity (left) poleward of -70^{o} latitude.

Plate 5. Overlays of stereographic projections of the Epi* neutron flux and Clementine 750 nm intensity poleward of $+70^{o}$ (left) and -70^{o} (right) latitudes.

Figure 1. MCNP simulations of neutron flux for temperatures between 25K and 400K under the assumption of a constant FAN composition. At the top is an overview showing the dominant temperature variation at thermal energies. At the bottom is a blow-up of the epithermal energy range that shows systematic variations in this range as well.

Figure 2. Simulation of the variation of counting rates using the flux functions in Figure 1 and the energy-dependent LP HeCd sensor efficiency function.

Figure 3. Simulation of the latitude, λ, variation of epithermal neutron flux (normalized to the equator) under the assumption of a $Cos^{1/4}\lambda$ temperature dependence and a constant FAN composition.

Figure 4. Latitude variations of Epi* counting rates within 1^{o}-wide bands averaged over 18 bands separated by 10^{o} longitude intervals at the equator.

Figure 5. A sample of six 1^{o}-wide Epi* counting rate bands that highlight several surface features See the text for details.

Figure 6. Scatter plots of the hydrogen abundance estimated from Epi* counts at the centers of 14 large craters pole-ward of $\pm 70^{o}$ latitude, and the maximum (top) and average (bottom) temperatures of these craters as estimated from the simulations of Vasavada et al. [1999].

Figure 7. Variation of diffusion time scales as a function of temperature for a selection of minerals. See the text for details.

Figure 8. Scatter plots of the hydrogen abundance estimated from Epi* counts at the centers of 14 large craters pole-ward of $\pm 70^{o}$ latitude, and the diffusion times estimated for olivine at the maximum (top) and average (bottom) temperatures estimated from the simulations of Vasavada et al. [1999].

Table 1

Hydrogen Abundance and Diffusion Time Scales of Various Lunar Features

Crater	**N Lat**	**E Long.**	**% Epi* Diff**	**[H] (ppm)**	**T_a. (K)**	**$Log_{10}[T_d(T_a)]$**	**T_m (K)**	**$Log_{10}[T_d(T_m)]$**
Th < 3ppm	75	360	0.0	55.4	250	-0.334	390	-9.78
North Pole	90	360	-6.3	160	14.9		160	15.24
South Pole	-90	360	-6.1	160	14.9		160	15.24
Tycho	-43	-11	+2.7	6.4	231.2	1.873	360.7	-8.36
Jackson	22	-164	+2.4	11.6	245.3	0.186	382.7	-9.45
Max Epi* Cts	46	110	+3.0	0.0	228	2.285	356	-8.12
Hermite	86	270	-3.2	116	145	19.32	219	3.81
Peary (max)	88	20	-6.4	145	19.3		195	7.62
Between P&R	85	170	-8.0	147	18.7		225	2.98
Rozhdestvenskiy	85	-150	-3.8	126	147	18.69	225	2.982
Plaskett	82	175	-3.9	129	152	17.17	249	0.0759
Milankovic	77	170	-1.5	83	165	13.65	275	-2.50
Karpinskiy	73	165	-0.88	71.8	172	11.98	290	-3.78

Byrd	85	4	-2.9	110	147	18.69	225	2.98
Nansen	81	93	-2.6	104	160	14.93	254	-0.461
Goldschmidt	73	134	-1.3	80.2	172	11.98	290	-3.78
Shoemaker-Faustini	-88	60	-6.7	1700	100	40.38	100	40.68
Cabeus	-84	-40	-7.5		100	40.4	100	40.68
Drygalski	-79	-89	-0.73	69.1	162	14.41	264	-1.47
Ashbrook	-82	-115	-1.1	76	152	17.17	249	0.0761
Schroedinger	-75	134	-1.3	80.2	170	12.44	285	-3.37
Scott	-82	46	0.0	55.4	152	17.17	249	0.076
Demonax	-79	60	-0.15	58.1	162	14.41	264	-1.47
Zeeman	-75	-140	0.0	55.4	170	12.44	285	-3.37

Table 2

Plasma Proton Properties of the Earth's Magnetosheath and Plasma Sheet

Parameter	**Solar Wind**	**Magnetosheath**	**Plasma Sheet**
Density, N, cm^{-3}	8.7	6.0	0.1
Bulk Velocity, V_o, km s^{-1}	468	420	low
Thermal Speed, V_T, km s^{-1}	44.5	73	875
$(\delta V^2)^{1/2}$, km s^{-1}	20.5	35	low
Thermal Mach #, M	10.5	6.1	low
Effective δV^*, km s^{-1}	49.0	81	875
Effective Mach #, M*	9.6	5.5	low
Proton Flux, NV_o, cm^{-2} s^{-1}	3.8×10^8	2.4×10^8	8.8×10^6

Table 3

Characteristic Surface Time Scales

Scale Type	Time, years
Initial Deposition Time	$5x10^3$
Diffusion Time (Olivine @ 250 K)	$4x10^8$
Time Exposed to Plasma Environment	$1.5x10^5$
Time Above Surface Skin Depth, 2 cm	$1x10^7$
Polar Orientation Time	2 to 3 $x10^9$

Table 4

Diffusion Constants for Selected Minerals

Mineral	D_o, $m^2\ s^{-1}$	Q, kJ $(g\ mole)^{-1}$	Reference
Olivine	$6x10^{-5}$	130	Mackwell and Kohlstedt, 1990
Quartz	$5x10^{-4}$	176	Kats et al., 1962
Quartz	$1.4x10^{-1}$	200	Kronenberg et al., 1986
Potassium Feldspar	$6.2x10^{-4}$	172	Kronenberg et al., 1989
Rutile (‖ c axis)	$1.8x10^{-7}$	60	Johnson et al., 1995
Rutile (⊥ c axis)	$3.8x10^{-5}$	120	Johnson et al., 1995
Pyrope	1.77	253	Wang et al., 1996
Basalt melt	$3.76x10^{-6}$	126	Zhang and Stolper, 1991
Diopside	$5.04x10^{-7}$	136	Ingrin et al., 1995
Rhyolite	$4.61x10^{-7}$	103	Zhang, et al., 1991

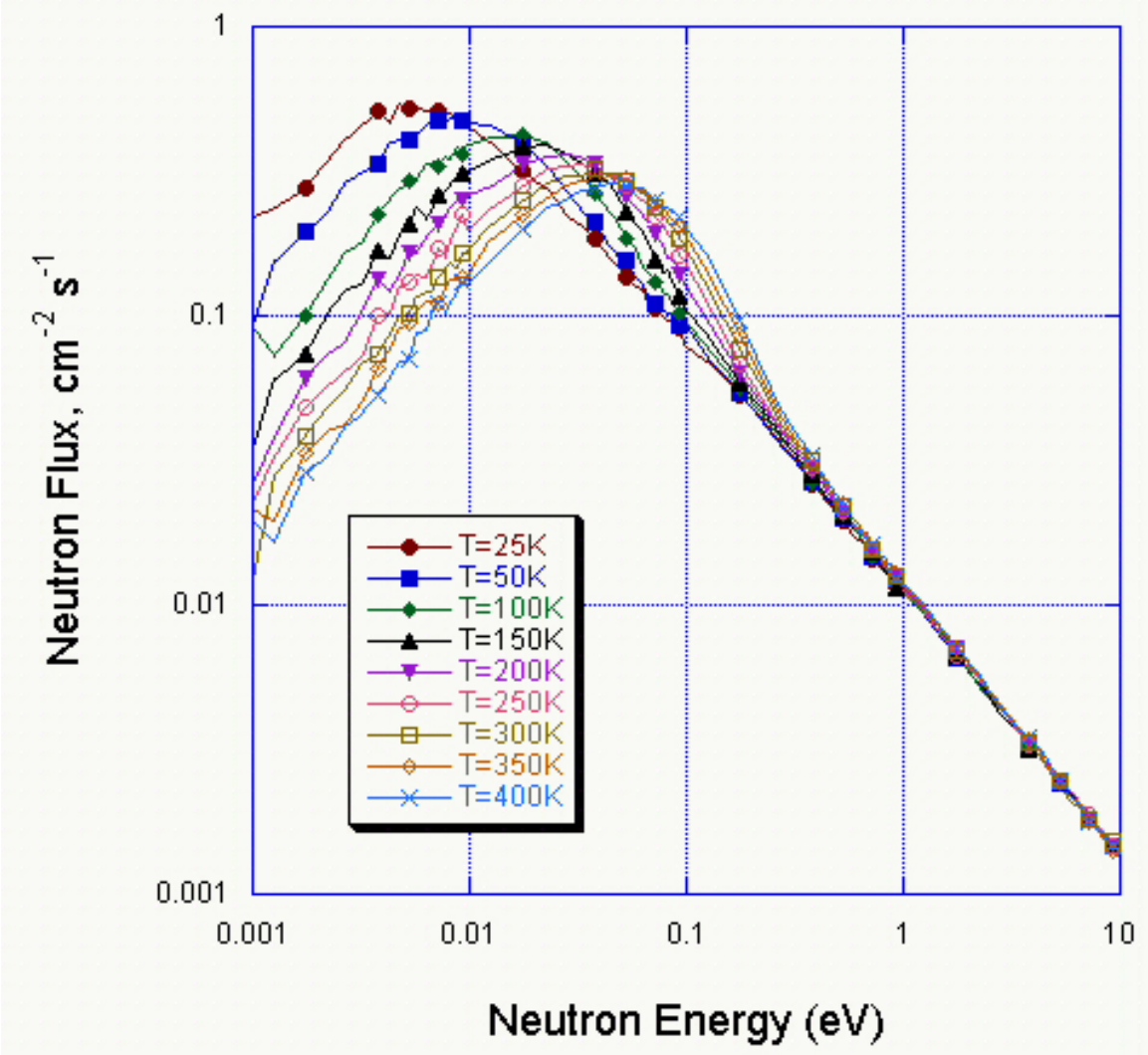
Neutron Flux, cm^{-2} s^{-1}
1
0.1
0.01
0.001
0.001
0.01
0.1
1
10
Neutron Energy (eV)
T=25K
T=50K
T=100K
T=150K
T=200K
T=250K
T=300K
T=350K
T=400K

Figure 1a

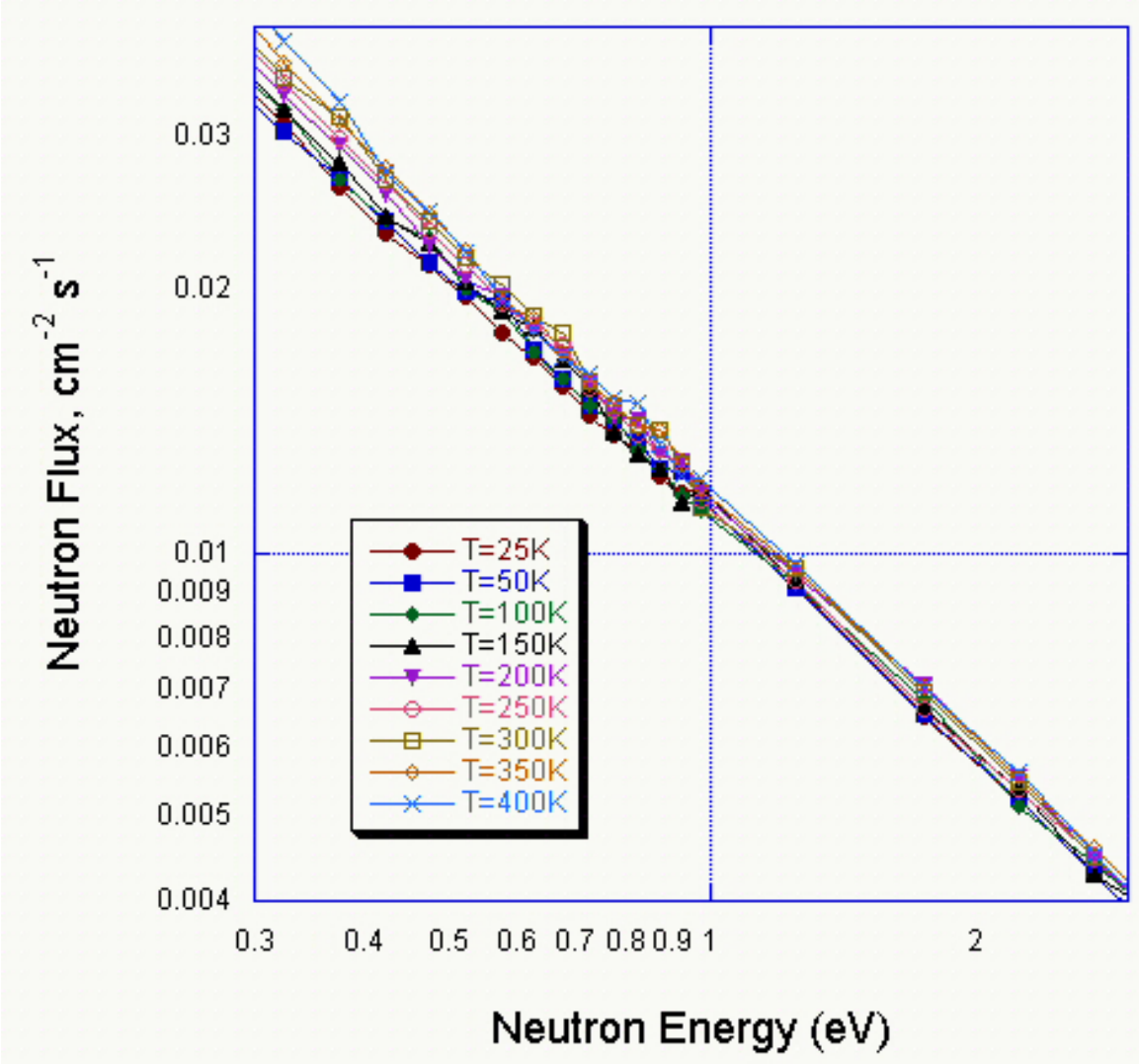
Neutron Flux, cm^{-2} s^{-1}
0.03
0.02
0.01
0.009
0.008
0.007
0.006
0.005
0.004
0.3
0.4
0.5
0.6
0.7
0.8
0.9
1
2
Neutron Energy (eV)
T=25K
T=50K
T=100K
T=150K
T=200K
T=250K
T=300K
T=350K
T=400K

Figure 1b

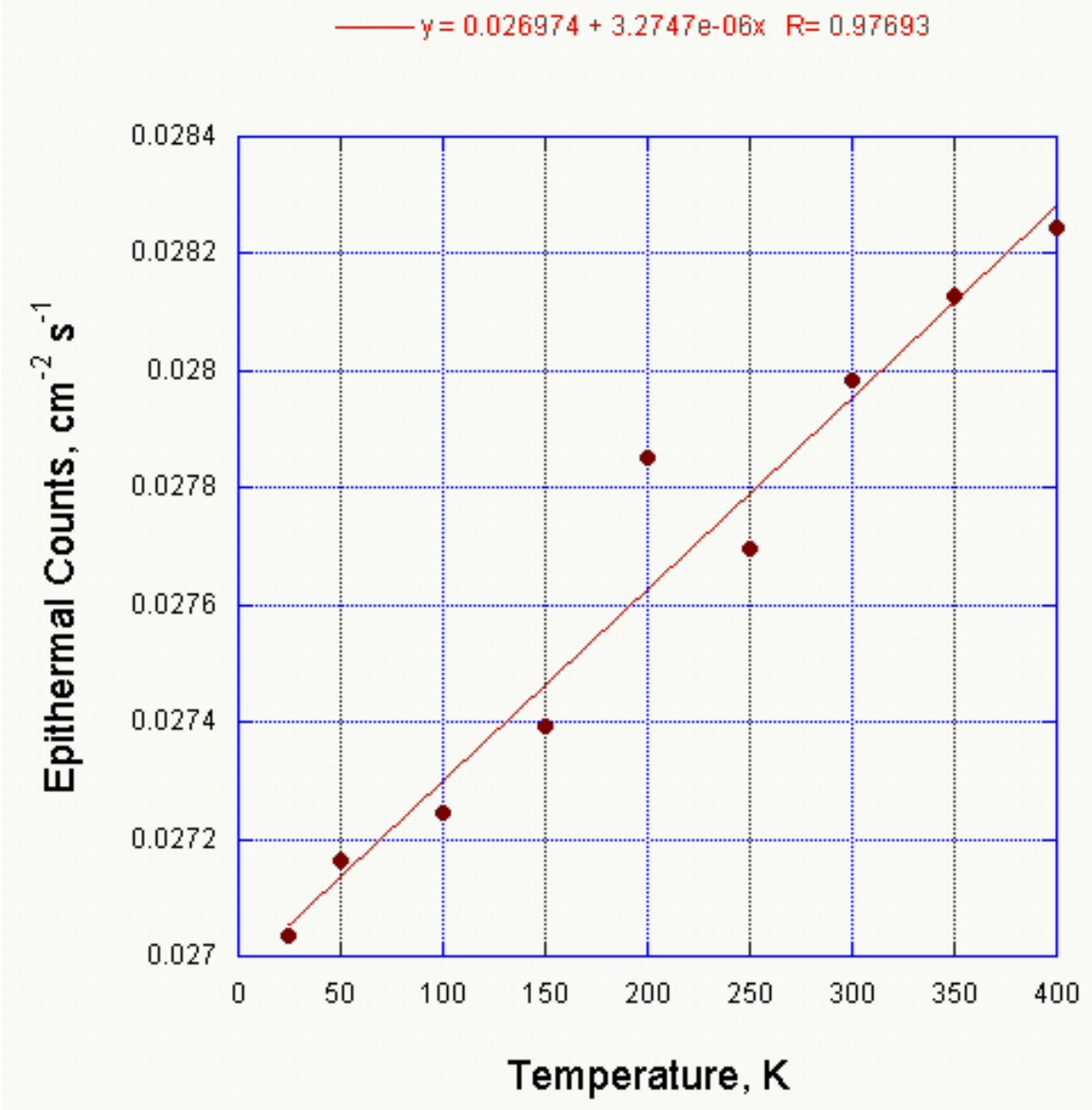
y = 0.026974 + 3.2747e-06x R= 0.97693
Epithermal Counts, cm-2 s-1
0.0284
0.0282
0.028
0.0278
0.0276
0.0274
0.0272
0.027
0
50
100
150
200
250
300
350
400
Temperature, K

Figure 2

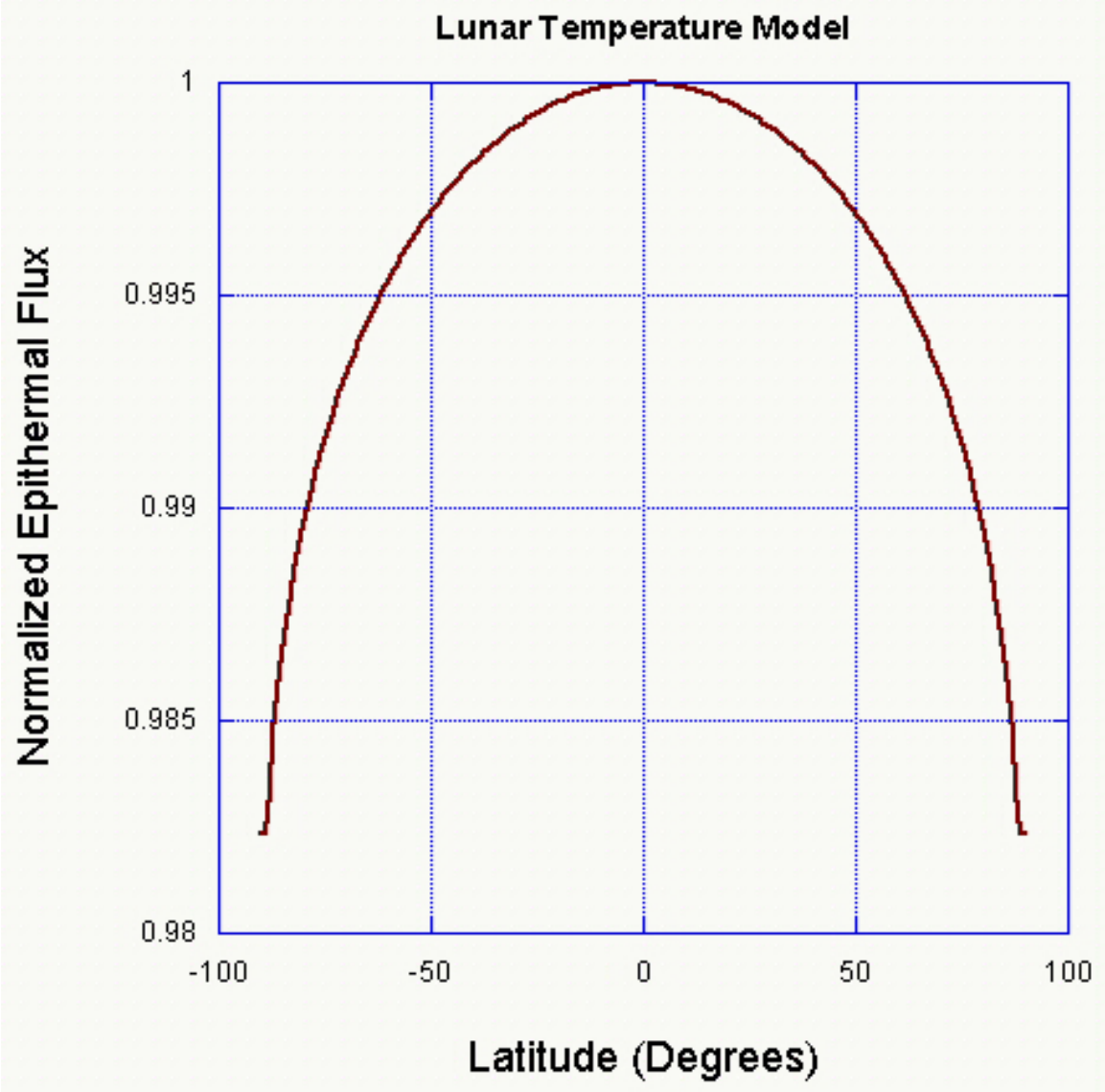
Lunar Temperature Model
Normalized Epithermal Flux
1
0.995
0.99
0.985
0.98
-100
-50
0
50
100
Latitude (Degrees)

Figure 3

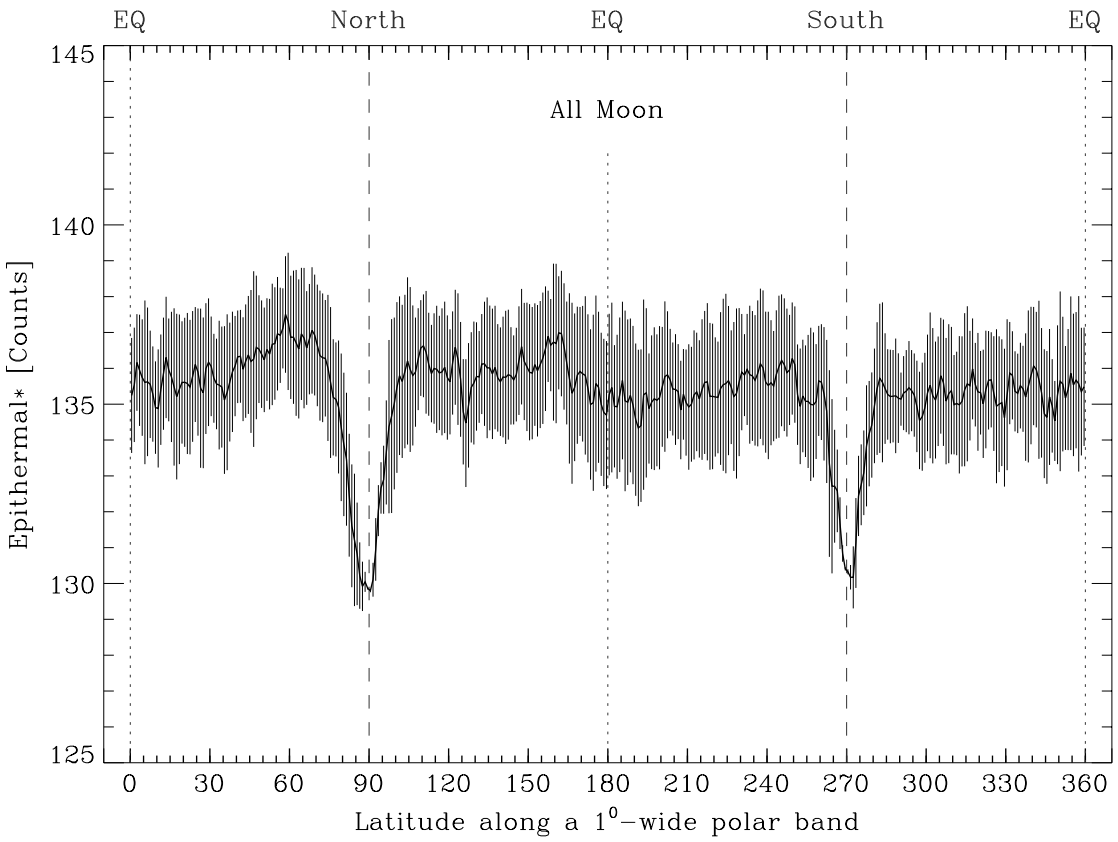
EQ
North
EQ
South
EQ
All Moon
Epithermal* [Counts]
145
140
135
130
125
0
30
60
90
120
150
180
210
240
270
300
330
360
Latitude along a 1⁰–wide polar band

Figure 4

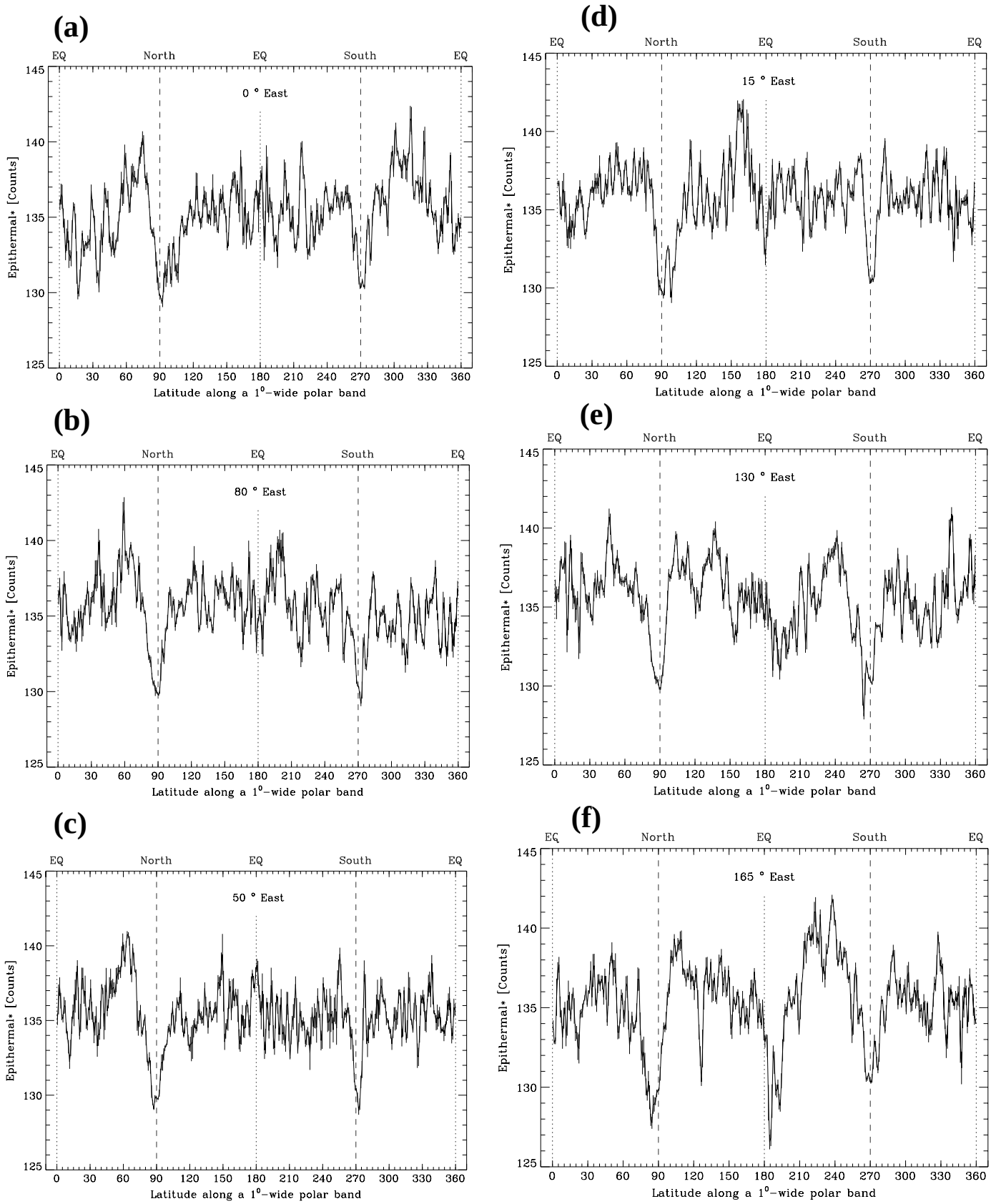
(a)
EQ North EQ South EQ
0 ° East
Epithermal* [Counts]
Latitude along a 1°–wide polar band
(b)
80 ° East
(c)
50 ° East
(d)
15 ° East
(e)
130 ° East
(f)
165 ° East

Figure 5

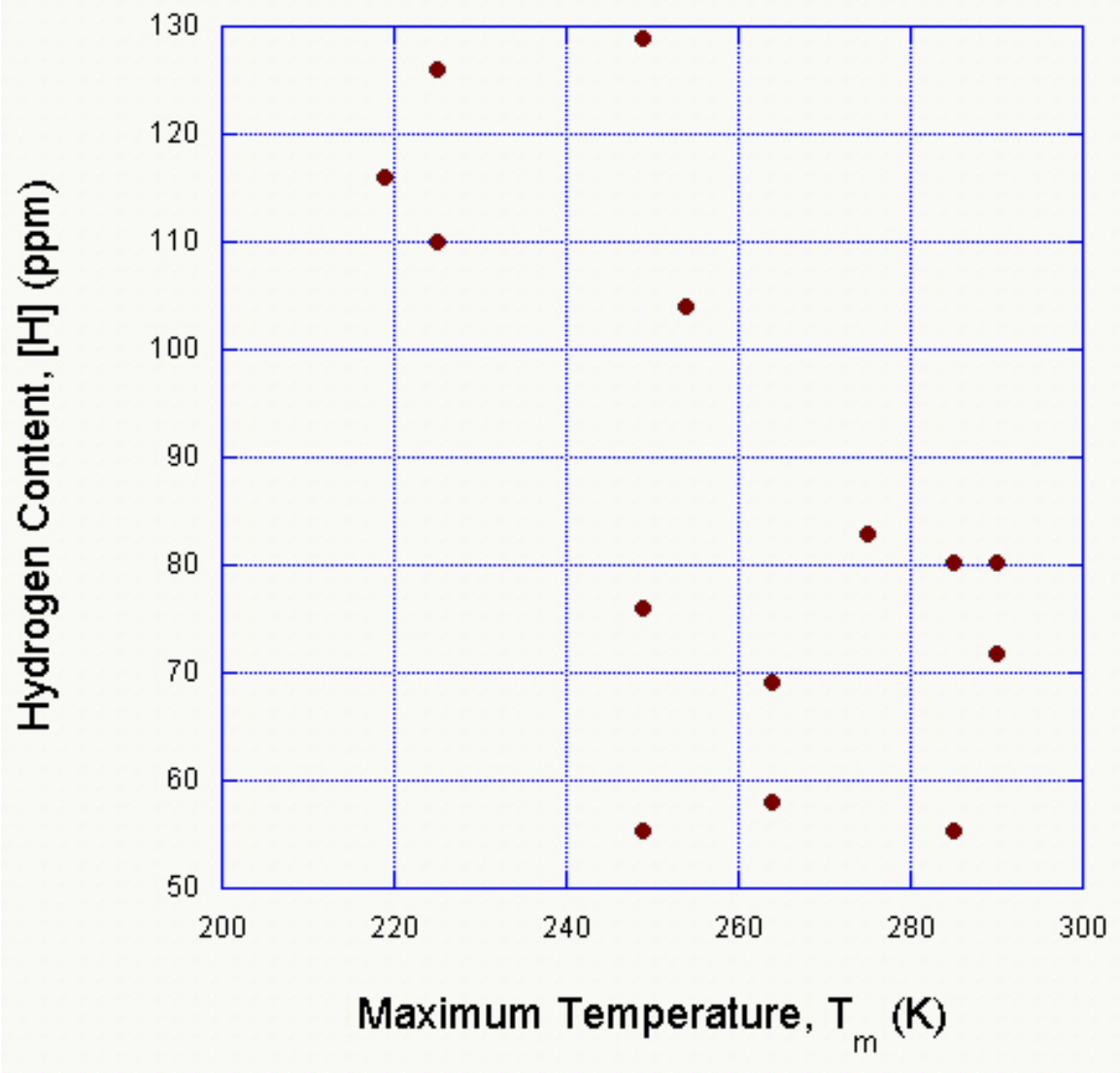
Hydrogen Content, [H] (ppm)
130
120
110
100
90
80
70
60
50
200
220
240
260
280
300
Maximum Temperature, T m (K)

Figure 6a

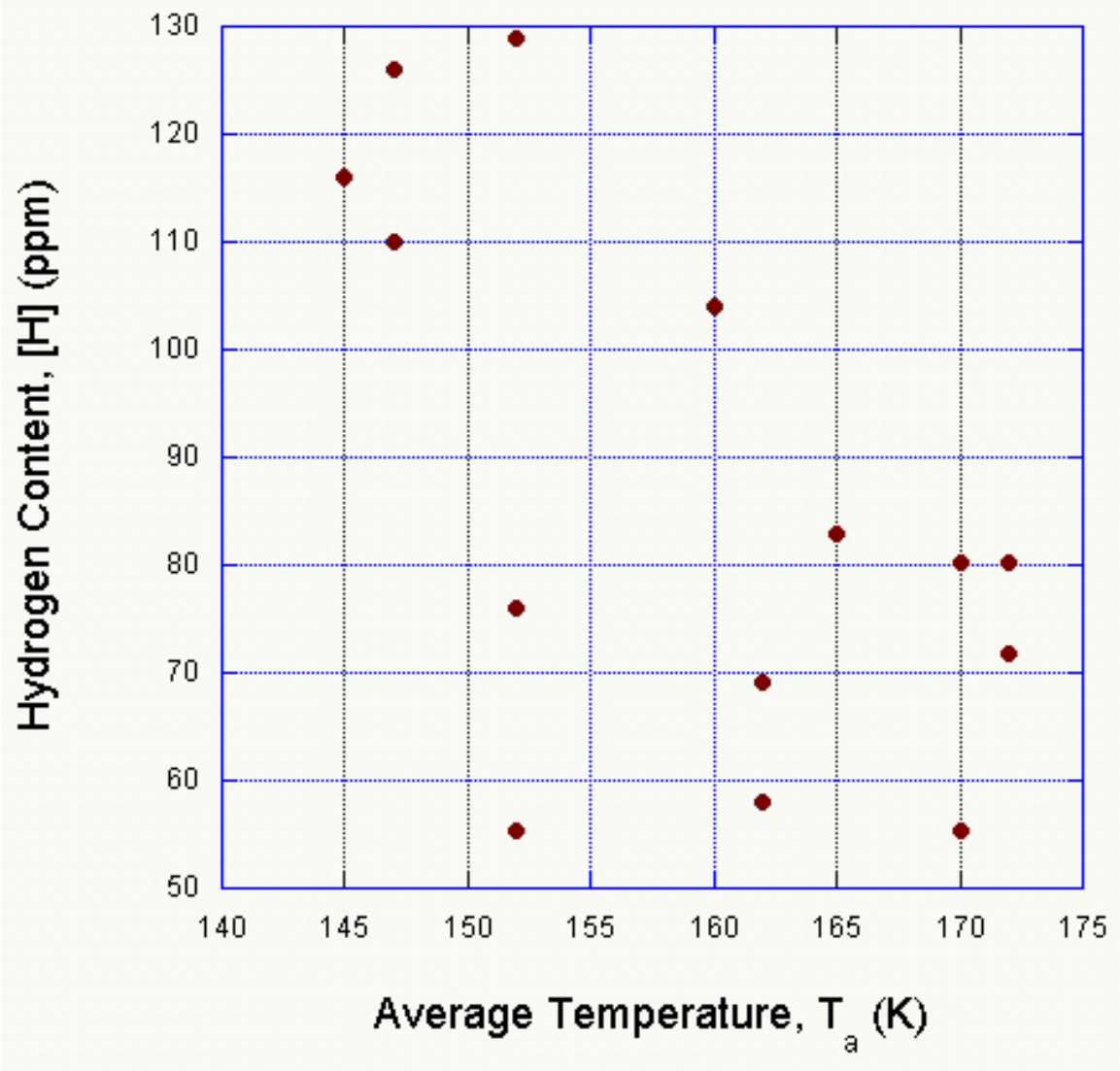
Hydrogen Content, [H] (ppm)
130
120
110
100
90
80
70
60
50
140
145
150
155
160
165
170
175
Average Temperature, T a (K)

Figure 6b

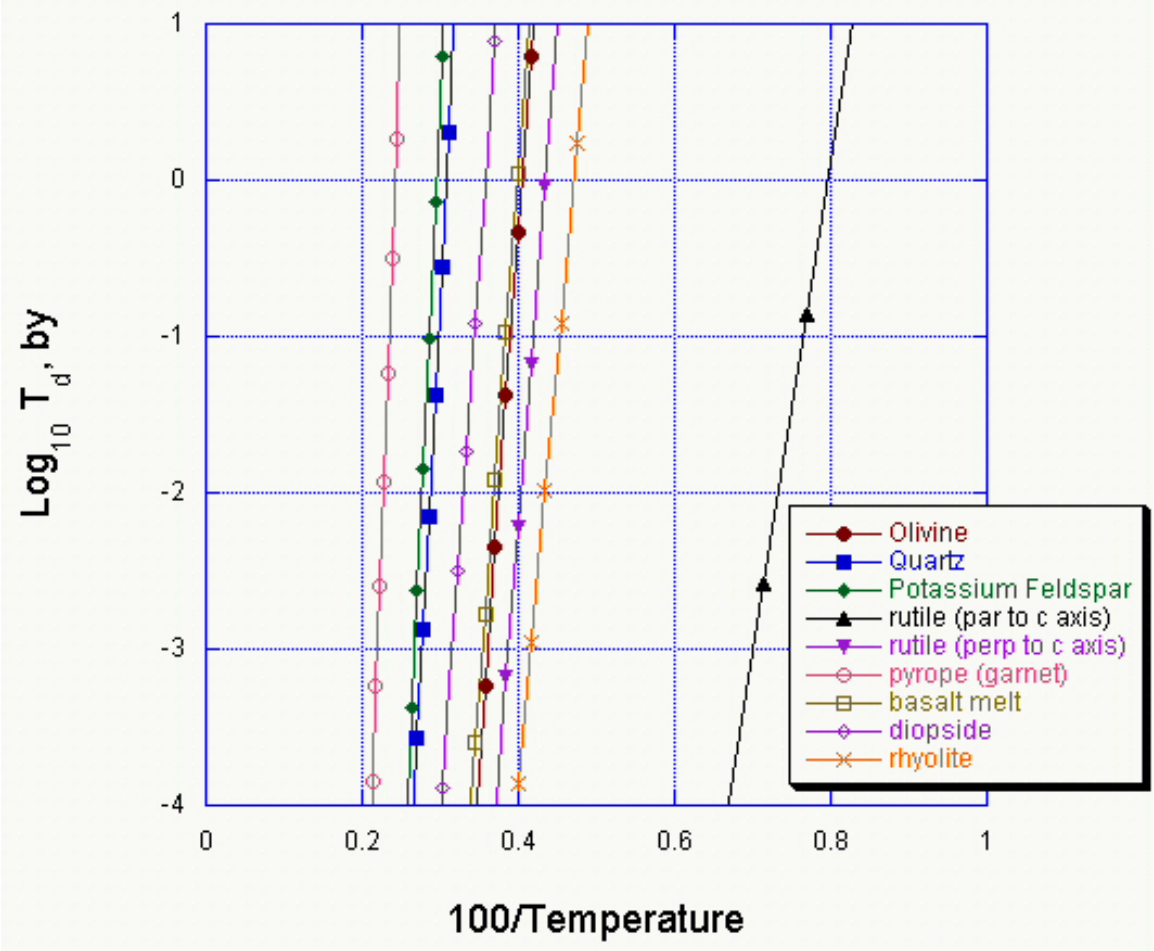
1
0
-1
-2
-3
-4
0
0.2
0.4
0.6
0.8
1
Log10 Td', by
100/Temperature
Olivine
Quartz
Potassium Feldspar
rutile (par to c axis)
rutile (perp to c axis)
pyrope (garnet)
basalt melt
diopside
rhyolite

Figure 7

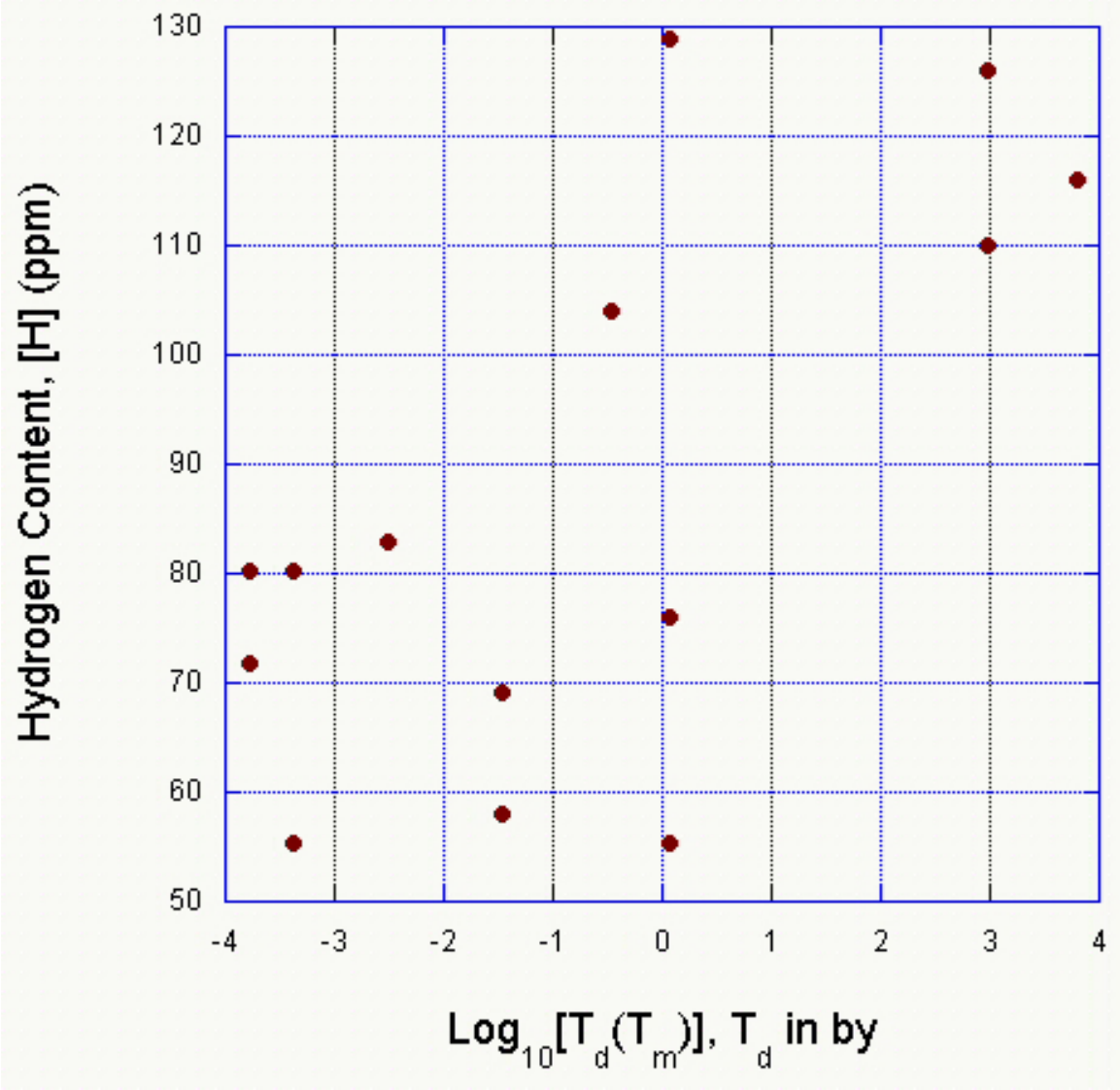
Hydrogen Content, [H] (ppm)
130
120
110
100
90
80
70
60
50
-4
-3
-2
-1
0
1
2
3
4
Log10[Td(Tm)], Td in by

Figure 8a

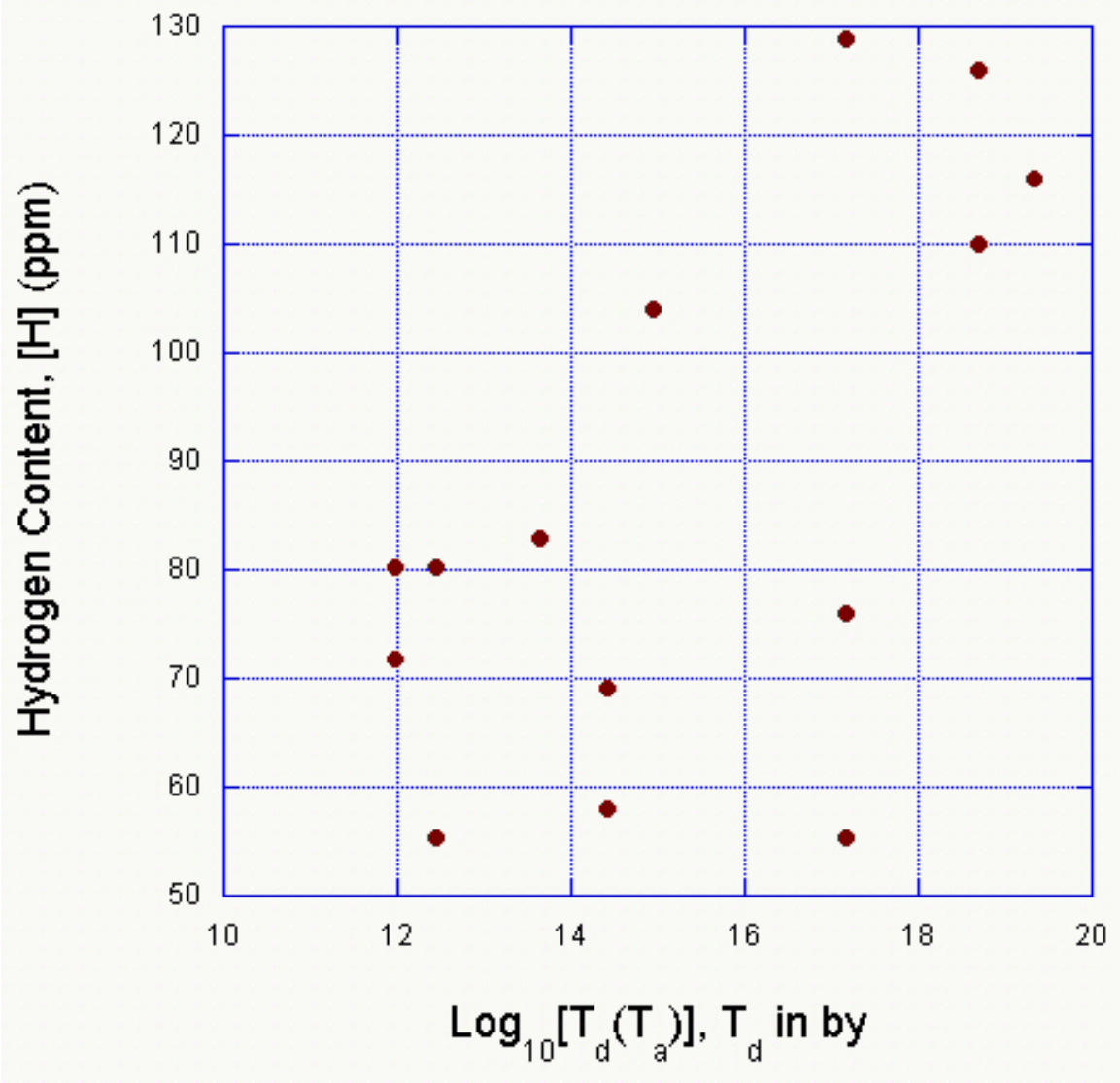
Hydrogen Content, [H] (ppm)
130
120
110
100
90
80
70
60
50
10
12
14
16
18
20
Log10[Td(Ta)], Td in by

Figure 8b

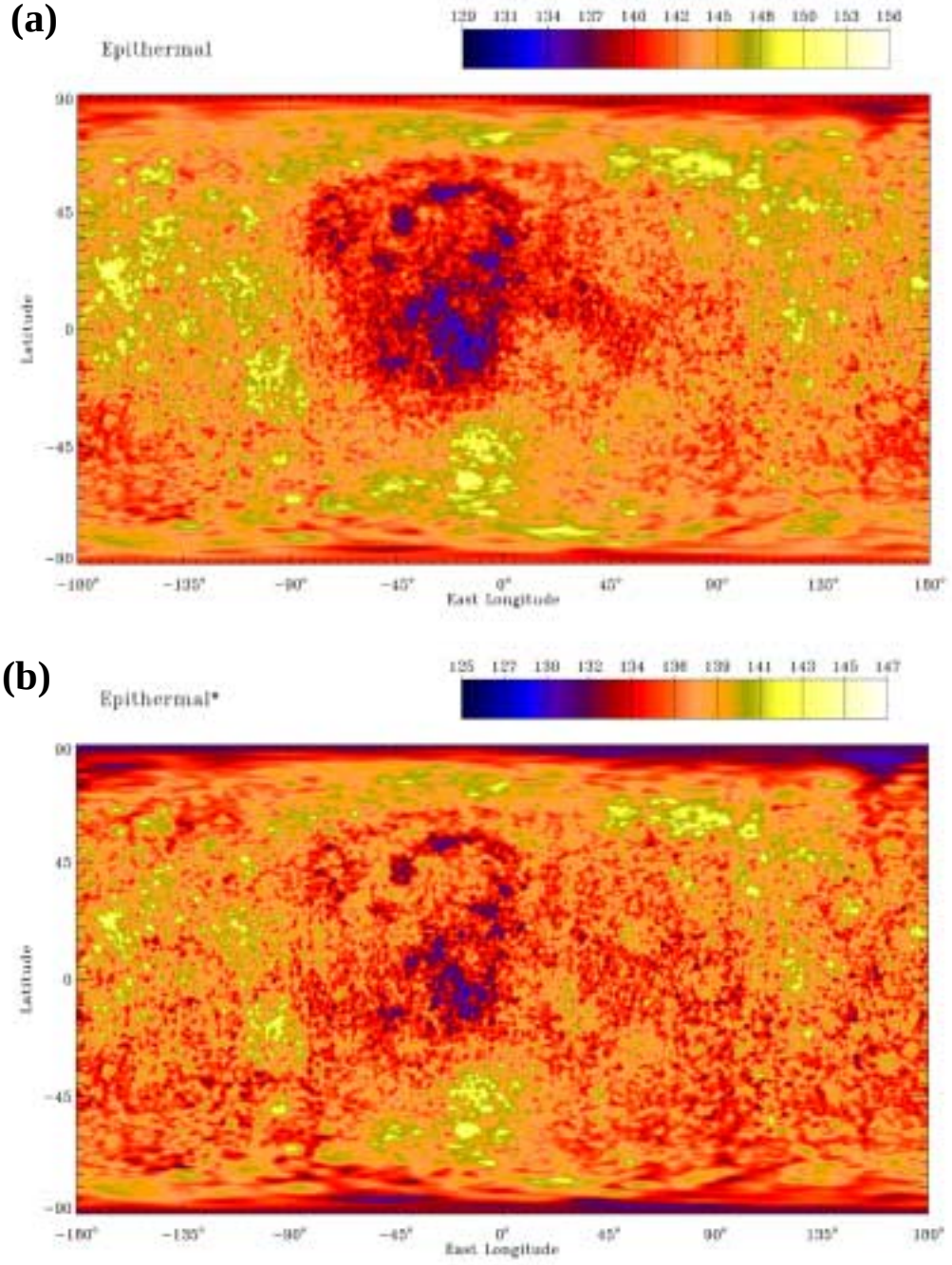
(a)
Epithermal
129 131 134 137 140 142 145 148 150 153 156
90
45
0
-45
-90
Latitude
-180° -135° -90° -45° 0° 45° 90° 135° 180°
East Longitude
(b)
Epithermal*
125 127 130 132 134 136 139 141 143 145 147
90
45
0
-45
-90
Latitude
-180° -135° -90° -45° 0° 45° 90° 135° 180°
East Longitude

Plate 1

(a)

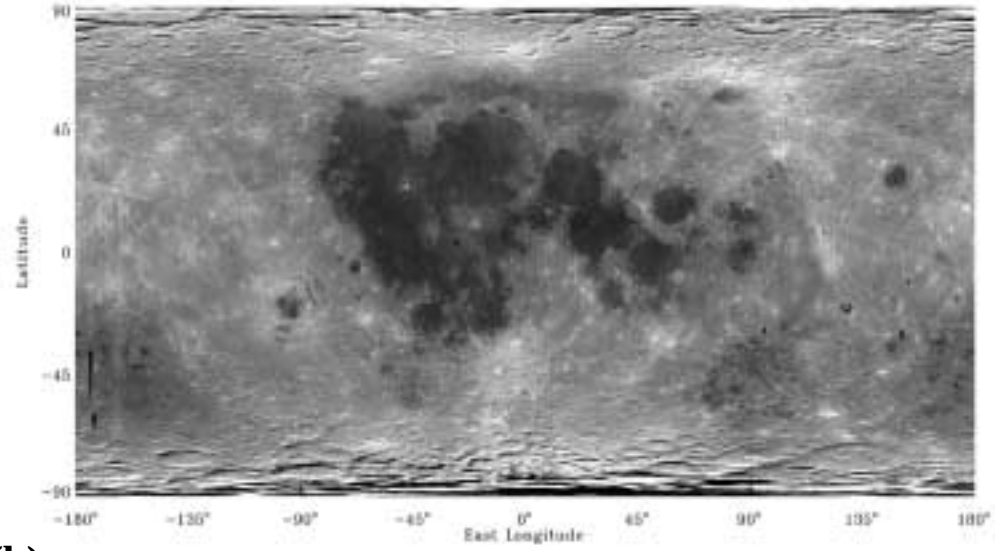
90
45
0
−45
−90
Latitude
−180°
−135°
−90°
−45°
0°
45°
90°
135°
180°
East Longitude

(b)

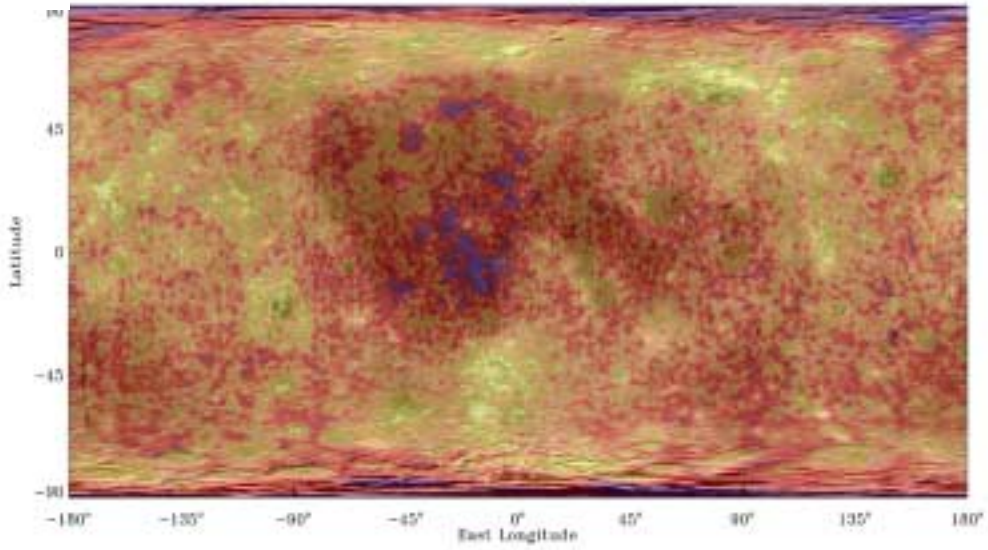
45
0
−45
−90
Latitude
−180°
−135°
−90°
−45°
0°
45°
90°
135°
180°
East Longitude

Plate 2

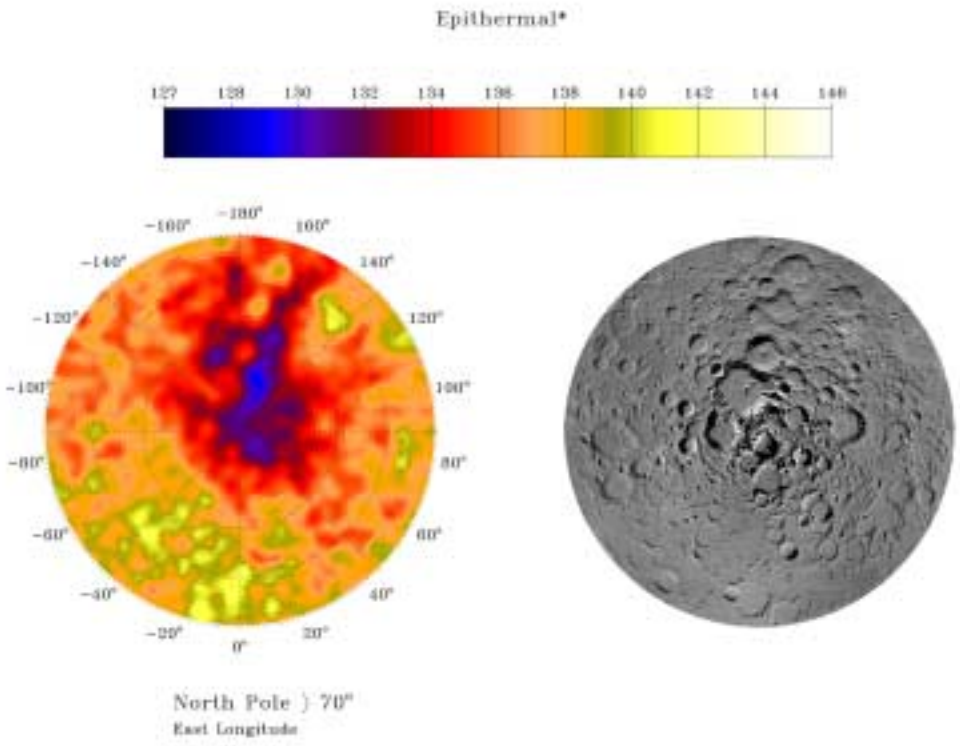
Epithermal*
127
128
130
132
134
136
138
140
142
144
146
-180°
-160°
-140°
-120°
-100°
-80°
-60°
-40°
-20°
0°
20°
40°
60°
80°
100°
120°
140°
160°
North Pole) 70°
East Longitude

Plate 3

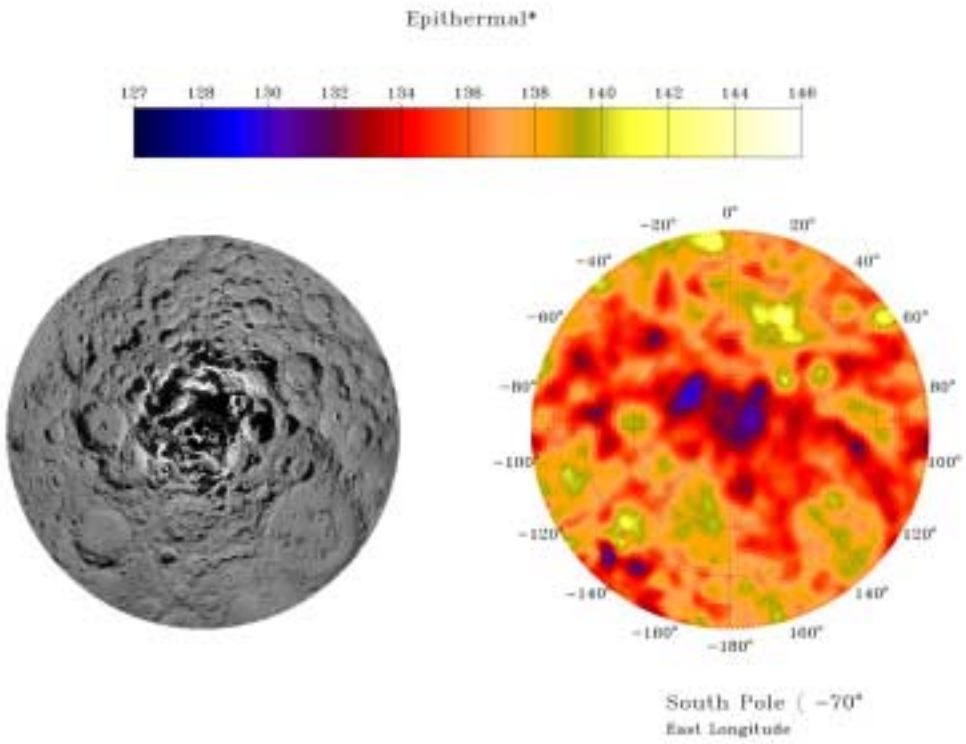
Epithermal*
127
128
130
132
134
136
138
140
142
144
146
0°
-20°
20°
-40°
40°
-60°
60°
-80°
80°
-100°
100°
-120°
120°
-140°
140°
-160°
160°
-180°
South Pole (-70°
East Longitude

Plate 4

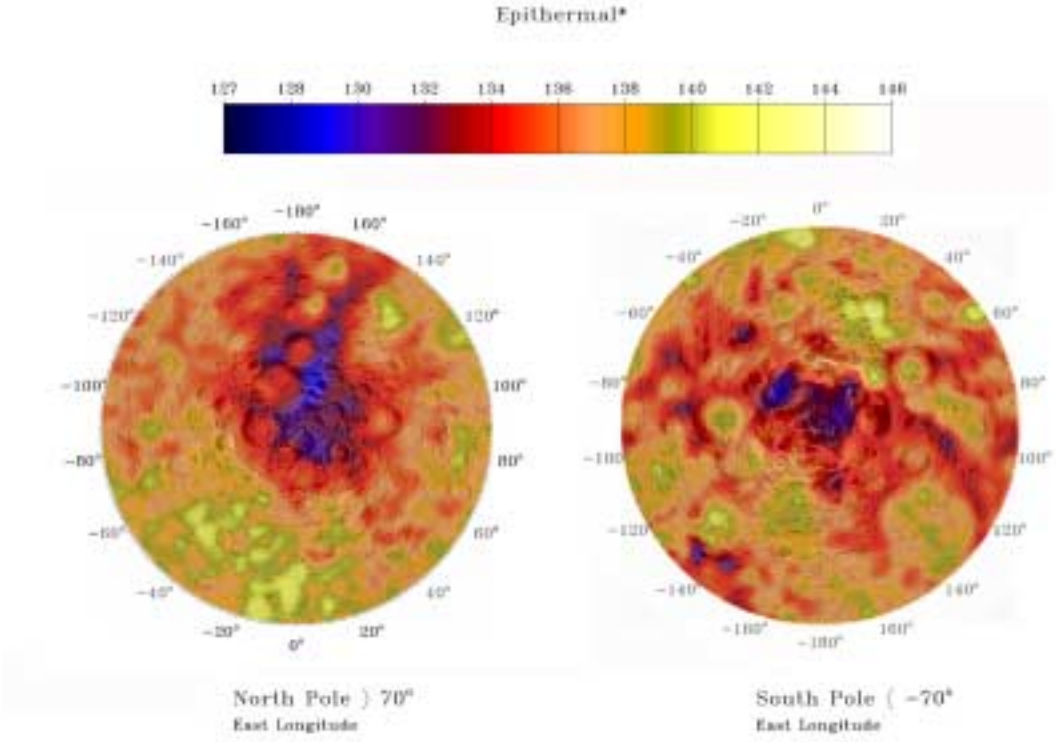
Epithermal*
127 128 130 132 134 136 138 140 142 144 146
North Pole) 70°
East Longitude
South Pole (-70°
East Longitude

Plate 5